

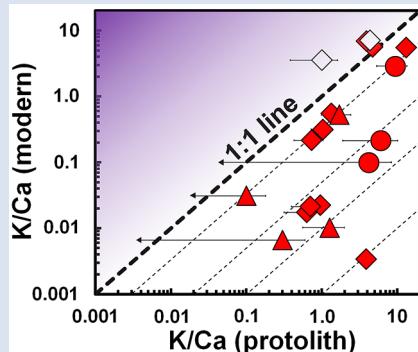
Radiogenic Ca isotopes confirm post-formation K depletion of lower crust

M.A. Antonelli^{1*}, D.J. DePaolo^{1,2}, T. Chacko³, E.S. Grew⁴, D. Rubatto⁵



doi: 10.7185/geochemlet.I904

Abstract



K/Ca suggest that 20–30 % minimum (granitic) melt removal can explain the K depletions.

Heat flow studies suggest that the lower crust has low concentrations of heat-producing elements. This could be due to either (i) greater fractions of basaltic rock at depth or (ii) metamorphic depletion of radioactive elements from rocks with more evolved (andesitic to granodioritic) compositions. However, seismic data suggest that lower crust is not predominantly basaltic, and previous studies (using Pb and Sr isotopes) have shown that lower crustal rocks have experienced significant losses of U and Rb. This loss, however, is poorly constrained for K, which is inferred to be the most important source of radioactive heat in the earliest crust. Our high precision Ca isotope measurements on a suite of granulite facies rocks and minerals from several localities show that significant losses of K (~60 % to >95 %) are associated with high temperature metamorphism. These results support models whereby reduction of heat production from the lower crust, and consequent stabilisation of continental cratons in the Precambrian, are largely due to high temperature metamorphic processes. Relative changes in whole rock

Received 18 October 2018 | Accepted 4 January 2019 | Published 6 February 2019

Introduction

Samples from lower continental crust (LCC) can be brought to the surface in two major ways, either (i) as coherent high grade terranes, through tectonic processes, or (ii) as individual xenoliths, through deep-seated volcanism. Based on analysis of these samples, it has been established that much of the LCC was heated to granulite facies conditions (>~800 °C) and lost significant amounts of its original heat producing element budget (Rudnick and Gao, 2014), yet it is uncertain whether this is a sufficient explanation for modern heat flow data without invoking greater fractions of mafic crust at depth (Hacker *et al.*, 2015).

Metamorphic heating results in the breakdown of primary hydrous mineral phases to anhydrous mineral assemblages. Typical reactions involve the transformation of amphibole and mica into feldspar, pyroxene, sillimanite/kyanite, and (at higher pressures) garnet. These transformations are typically accompanied by the generation of granitic liquids (rich in incompatible elements and containing dissolved H₂O) that are generally lost from the system, but found preserved as microscopic melt inclusions (*e.g.*, Bartoli *et al.*, 2016; Stepanov *et al.*, 2016; Ferrero *et al.*, 2018). There is also evidence that fluid loss in the absence of melt generation could contribute to the

geochemical changes, as suggested by the common observation of high Th/U in granulite facies rocks (Rudnick and Gao, 2014). Generation and loss of melt, however, is viewed in the more recent literature as being the primary mechanism affecting granulite and ultrahigh temperature (UHT) rocks (*e.g.*, White and Powell, 2002; Guernina and Sawyer, 2003; Kelsey and Hand, 2015). The lower U, Th, (and K) concentrations and higher density of LCC (Rudnick and Gao, 2014; Hacker *et al.*, 2015) could therefore be attributed to the effects of melt loss during high temperature (HT) metamorphism accompanied by anatexis.

Previous work suggesting that U is lost from LCC is based on Pb isotopes and by comparison with Th (Rudnick and Gao, 2014), which can also be lost during partial melting at extreme conditions (Ewing *et al.*, 2014; Stepanov *et al.*, 2014). However, ancient K-loss during melting of LCC is hard to constrain because there are few means to establish K content of the protoliths (Rudnick *et al.*, 1985). Previous studies show that Rb is preferentially lost during granulite facies metamorphism relative to Sr and K (DePaolo *et al.*, 1982; Rudnick *et al.*, 1985), and that there can also be K loss relative to Ca (Ewing *et al.*, 2014; Stepanov *et al.*, 2014). However, this argument has considerable uncertainty for K when the protoliths are unavailable for analysis, and the magnitude of K loss from

1. Department of Earth and Planetary Science, University of California - Berkeley, Berkeley, CA 94720, USA
 2. Lawrence Berkeley National Laboratory, Berkeley, CA 94720, USA
 3. Department of Earth and Atmospheric Sciences, University of Alberta, Canada
 4. School of Earth and Climate Sciences, University of Maine, USA
 5. Institute of Geological Sciences, University of Bern, Switzerland
- * Corresponding author (e-mail: Mantonelli@berkeley.edu)



LCC remains poorly constrained. To address this problem, we use measurements of radiogenic ^{40}Ca in lower crustal granulite facies rocks and minerals. The K-Ca system is well-suited for this purpose because ^{40}K decays to ^{40}Ca (and ^{40}Ar , $t_{1/2} \sim 1.25$ Gyr), the two elements are separated from each other during partial melting, and the daughter product is generally more compatible than the parent (Marshall and DePaolo, 1989).

Samples and Analytical Procedures

We report radiogenic ^{40}Ca variations (ϵ_{Ca}) in granoblastic to porphyroblastic mafic, granitic, and pelitic whole rocks and mineral separates from four localities: the Napier Complex, Antarctica (NC); the Slave Province, Canada (SP); the

Ivrea-Verbano Zone, Italy (IVZ); and the Lhasa Block, Tibet (Sumdo eclogite, SE). The rocks span a wide range of chemical compositions and metamorphic pressure and temperature conditions, including granulite/UHT ($n = 17$), amphibolite ($n = 3$), and eclogite facies ($n = 1$), and range in age from Archean to Mesozoic (Supplementary Information, SI, and Tables S-1 through S-4). The SE is not likely to have lost significant amounts of K and is included only for reference (Fig. 1). Ca isotopic compositions were measured by TIMS at the University of California, Berkeley, and are reported in epsilon notation relative to Bulk Silicate Earth (BSE, SI, Table S-5), according to Equation 1.

$$\epsilon_{\text{Ca}} = \left(\frac{\left[\frac{^{40}\text{Ca}}{^{44}\text{Ca}} \right]_{\text{measured}}}{\left[\frac{^{40}\text{Ca}}{^{44}\text{Ca}} \right]_{\text{BSE}}} - 1 \right) \times 10^4 \quad \text{Eq. 1}$$

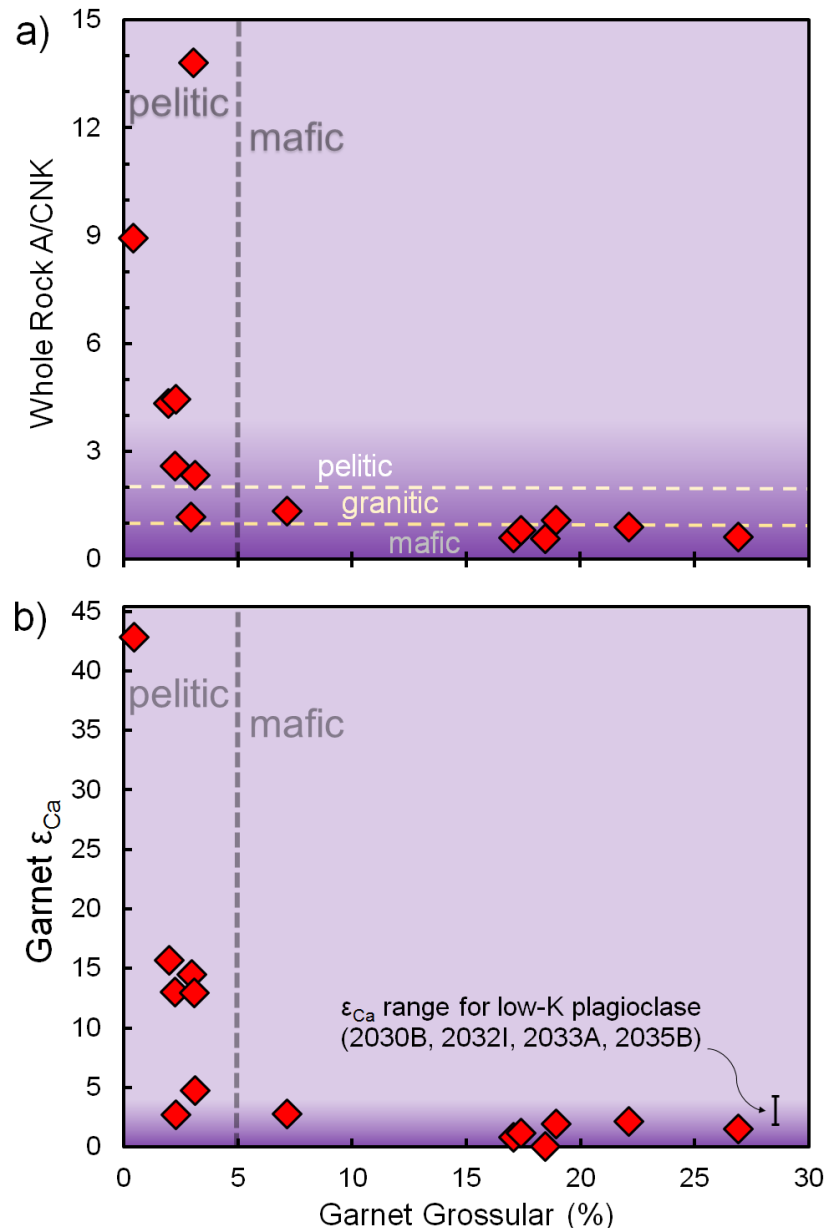


Figure 1 Garnet grossular content versus (a) whole rock peraluminosity index (A/CNK) and (b) garnet ϵ_{Ca} values (for samples containing garnet, $n = 14$). 2σ uncertainties (± 1 for ϵ_{Ca}) are smaller than the symbols. Approximate mafic, granitic, and pelitic compositional zones are separated by dashed lines (SI). Darker purple band in (b) represents Bulk Silicate Earth ($\epsilon_{\text{Ca}} = 0$) composition, corresponding to $^{40}\text{Ca}/^{44}\text{Ca} = 47.156$ (SI).

ϵ_{Ca} in Low-K Metamorphic Rocks and Minerals

Garnet is an ideal mineral for ϵ_{Ca} analyses because it effectively excludes K, is easy to separate, and commonly contains substantial amounts of Ca. Given a clean mineral separation, any excess radiogenic Ca in garnet must be inherited from ^{40}K that decayed to ^{40}Ca in the protolith, prior to garnet formation. We find that clean garnet separates have ϵ_{Ca} ranging from 0 to +42 (Table S-5). Higher ϵ_{Ca} values are found in garnets with lower grossular content [molar Ca/(Ca+Fe+Mg+Mn) < ~5 %], from rocks with generally higher whole rock peraluminosity [defined as molar Al_2O_3 /(CaO+Na₂O+K₂O) and denoted A/CNK in Fig. 1a]. In mafic granulites, both garnet and low-K plagioclase separates (which were sampled in the absence of garnet), have a narrow ϵ_{Ca} range from 0 to +3 (Fig. 1b). Whole rock and high-K feldspar separates were also measured (Fig. S-1) in order to obtain rough K-Ca isochrons (Fig. S-2), which are in general agreement with more precise dating methods for the various regions (SI).

Protolith K/Ca Estimates

Large depletions in K associated with metamorphism can be detected with our data on garnet mineral separates. Garnet and whole rock measurements for 2040C (NC), for example, have indistinguishable (yet highly elevated) ϵ_{Ca} values (+12.5, see Table S-5) due to a nearly complete loss of K from the rock during metamorphism, resulting in a near zero K/Ca similar to that of garnet. For rocks where K-loss is less extreme,

protolith K/Ca values are evaluated from ϵ_{Ca} (garnet or low-K plagioclase/whole rocks, SI) and the time interval between protolith formation and granulite facies metamorphism.

Using the metamorphic and protolith ages for each locality ('two-stage-model', SI), we are able to estimate the protolith K/Ca values using Equation 2, adapted from Marshall and DePaolo (1989).

$$[K/\text{Ca}]_{\text{protolith}} = \frac{\epsilon_{\text{Ca}}(t_2) - \epsilon_{\text{Ca}}(t_1)}{Q_{\text{Ca}}(e^{\lambda_K t_1} - e^{\lambda_K t_2})} \quad \text{Eq. 2}$$

Where $\epsilon_{\text{Ca}}(t_2)$ and $\epsilon_{\text{Ca}}(t_1)$ are ϵ_{Ca} values at metamorphic age (t_2) and protolith age (t_1), respectively; λ_K is the total decay constant of ^{40}K (assumed 0.554 Gyr⁻¹), and Q_{Ca} (~1.0804) is a factor incorporating the branching ratio of ^{40}K decay and the abundances of ^{40}K , ^{44}Ca , and ^{40}Ca relative to BSE.

In Figure 2, we show the effect of protolith age uncertainty on $[K/\text{Ca}]_{\text{protolith}}$ for our NC samples, based on Equation 2. This equation provides a *minimum* constraint on $[K/\text{Ca}]_{\text{protolith}}$ values because of three assumptions implicit in our use of the equation: (i) the oldest protolith age estimates for the various localities, (ii) single stage evolution from BSE [$\epsilon_{\text{Ca}}(t_1) = 0$] to garnet ϵ_{Ca} values [$\epsilon_{\text{Ca}}(t_2)$], and (iii) that garnets form out of the bulk protolith Ca pool at the time of metamorphism. Younger protolith ages, multiple stages for $[K/\text{Ca}]_{\text{protolith}}$ (e.g., increases driven by weathering/metamorphic processes), and/or partial loss of radiogenic Ca from K-bearing minerals prior to garnet formation (through earlier melting events), would all require higher $[K/\text{Ca}]_{\text{protolith}}$ to reach the same initial ϵ_{Ca} values at the time of metamorphism.

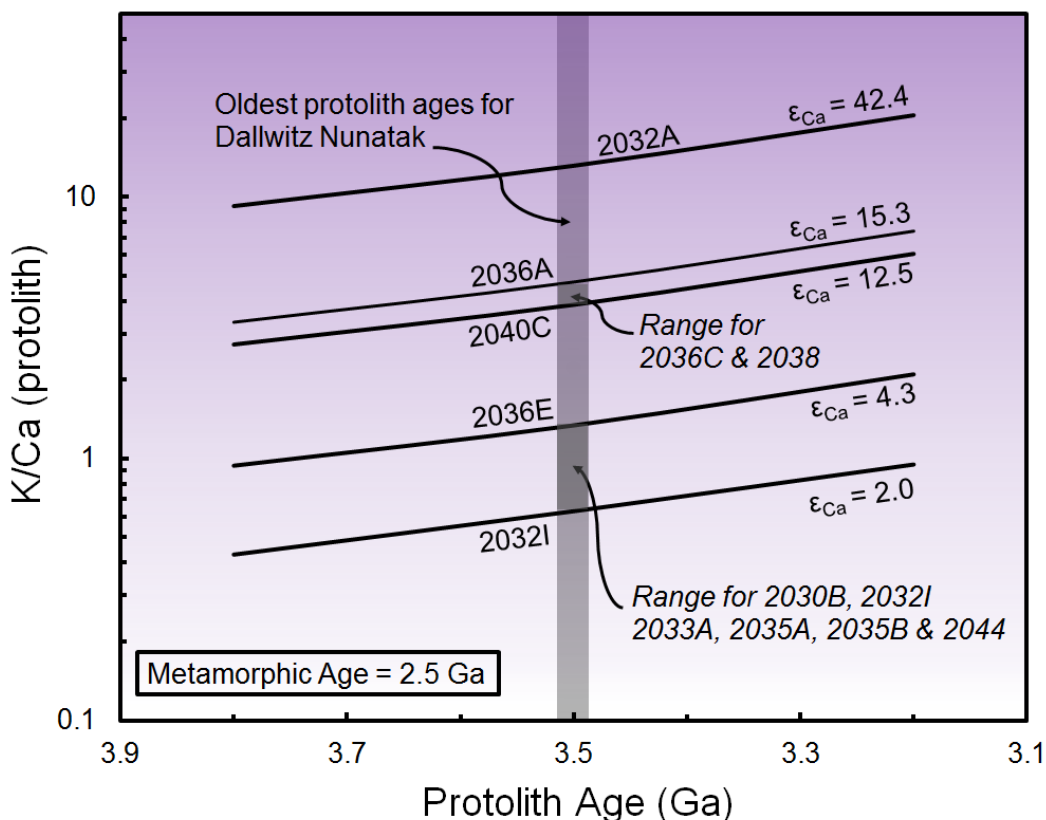


Figure 2 Dependence of $[K/\text{Ca}]_{\text{protolith}}$ on protolith age for samples from Dallwitz Nunatak (NC, n = 12) based on Equation 2. Curves are labelled by sample and delineate constant values for initial ϵ_{Ca} at 2.5 Ga with varying protolith ages. Grey band demarcates oldest protolith age found at Dallwitz Nunatak, in the northern Napier Complex (SI).

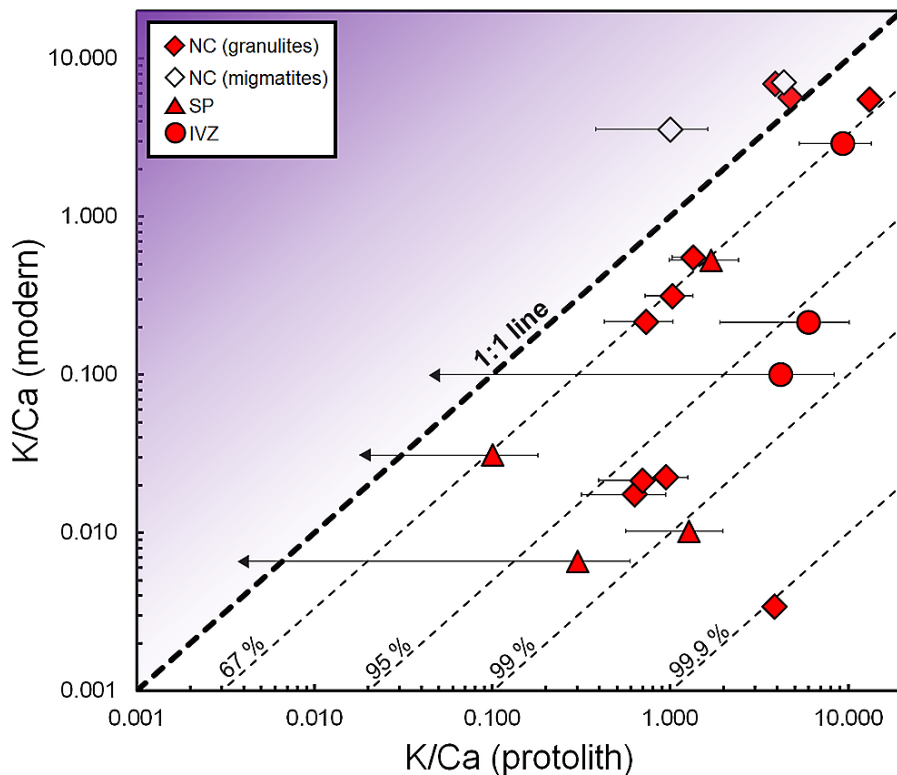


Figure 3 Whole rock K/Ca (modern) versus K/Ca (protolith) based on ϵ_{Ca} [Equation 2]. NC granulites ($n = 10$), NC migmatites ($n = 2$), SP ($n = 4$), IVZ ($n = 3$). Contours indicate relative K-loss (in %) assuming constant Ca. Uncertainties in protolith K/Ca are calculated using Equation 2, using our 2 sd on ϵ_{Ca} (± 1); arrow terminations represent samples within error of BSE. Protolith-metamorphic ages: 3.5–2.5 Ga (NC); 3.0–2.0 Ga (SP); and 0.6–0.3 Ga (IVZ) (SI). Uncertainties for modern K/Ca are $\sim 5\%$.

Potassium Loss during High-T Metamorphism

Including data from the other localities, we find as expected that mafic samples have lower $[\text{K}/\text{Ca}]_{\text{protolith}} < 1$, and pelitic samples have higher $[\text{K}/\text{Ca}]_{\text{protolith}}$ ranging from 1 to ~ 13 . Comparing these estimates with $[\text{K}/\text{Ca}]_{\text{modern}}$ in the whole rocks (Fig. 3), we are able to assess K-mobility during granulite metamorphism (see Fig. S-3 for data labels).

Our results indicate that most granulites have measured K/Ca that is substantially lower than that calculated for the protolith, indicating significant K-loss during metamorphism. The samples fall into 3 rough groups: one group has no K-loss, or a slight K enrichment, and the other groups cluster at 67 % and 97 %; one NC sample suggests greater than 99.9 % K-loss (Fig. 3). Samples with younger ages and lower ϵ_{Ca} have larger uncertainties. Two pelitic granulites and migmatites from the NC have an apparent increase in K/Ca relative to their protolith compositions, which can potentially be explained by the presence of (externally derived) captured melt. Our data suggest that granulite facies samples with less than ~ 2 wt. % modern whole rock K_2O have generally lost K, and samples with >2 wt. % have generally gained K (relative to Ca, Figure S-4). Although we are unaware of K-loss estimates for the NC and SP, our data agree with previous estimates for the IVZ, where granulite facies samples have about 2/3 less K than their lower temperature (amphibolite facies) counterparts (Ewing *et al.*, 2014). Our results are also in agreement with previous work on the Napier complex that found Pb and Sr isotope evidence for significant losses of Rb relative to Sr and U relative to Th (*e.g.*, DePaolo *et al.*, 1982; Kelsey and Hand, 2015).

Melt-loss Modelling

Although there is still some debate as to whether or not granulites need externally derived fluids in order to initiate melting (Aranovich *et al.*, 2016; Clemens *et al.*, 2016), the conclusion from melting experiments (Gao *et al.*, 2016) and from trapped melt inclusions in peritectic minerals (Bartoli *et al.*, 2016; Stepanov *et al.*, 2016; Ferrero *et al.*, 2018) is that granulites are often associated with loss of granitic melt. Given that we can quantify relative K/Ca decreases, we are also able to place constraints on the amount of melt loss required to form our samples by modelling the partitioning of K and Ca between melt and residual minerals.

To estimate K/Ca fractionation during partial melting, we use a modified non-modal batch melting model, where the bulk distribution coefficient for K (D_K) is a function of the mass fraction of remaining residual K-feldspar (the most significant K-bearing mineral at granulite facies conditions), and the bulk distribution coefficient for Ca (D_{Ca}) is a function of the mass fraction of residual plagioclase + clinopyroxene (SI, Fig. S-5).

Model Results

Comparing our model estimates for $[\text{K}/\text{Ca}]_{\text{solid}}/[\text{K}/\text{Ca}]_0$ versus $[\text{K}_2\text{O}]_{\text{solid}}$ (at various values of F) to our ϵ_{Ca} -based $[\text{K}/\text{Ca}]_{\text{mdrn}}/[\text{K}/\text{Ca}]_{\text{protolith}}$ estimates and $[\text{K}_2\text{O}]_{\text{mdrn}}$ analyses for granulite facies samples, and assuming that melt is completely lost from the system, we find that most of the samples are consistent with 20–30 % melting, with the most extreme sample suggesting melt fractions of $\sim 50\%$ (Fig. 4). Although the distribution coefficients used in our model are currently rough estimates, varying K and Ca distribution coefficients over a range of likely values (Fig. S-6) does not significantly change the results, which depend most significantly on $[\text{K}/\text{Ca}]_{\text{protolith}}$.



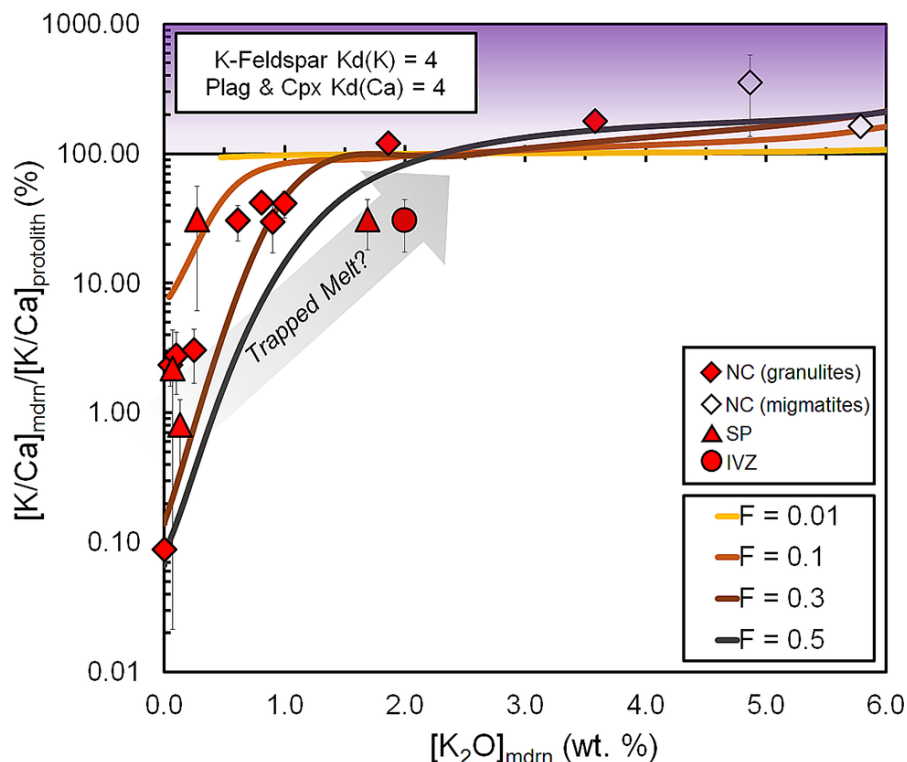


Figure 4 ϵ_{Ca} -based $[\text{K}/\text{Ca}]_{\text{mdrn}}/[\text{K}/\text{Ca}]_{\text{protolith}}$ [Equation 2] versus measured $[\text{K}_2\text{O}]_{\text{mdrn}}$ (excluding amphibolites and eclogites). Predictions from our melting model [Equations S-2 through S-4], for various starting compositions (same as in Fig. S-5) varying degree of partial melting (F) (coloured lines). NC granulites ($n = 10$), NC migmatites ($n = 2$), SP ($n = 4$), IVZ (IV-16-24, $n = 1$). Vertical error bars calculated using Equation 2, combining with those from XRF (<~5 % for $\text{K}_2\text{O}/\text{CaO}$); horizontal error bars are smaller than the symbols. Arrow shows effect of trapped melt on residual solids. Samples plotting above 100 % are consistent with model predictions for high K/Ca protoliths, but petrographic evidence (see SM) suggests that these potential enrichments result from (externally derived) trapped melt.

The model results generally agree with other approaches for estimating melt production during granulite facies metamorphism, including pseudosection analyses (White and Powell, 2002; Redler *et al.*, 2012; Yakymchuk and Brown, 2014; Green *et al.*, 2016; Palin *et al.*, 2016) and other methods (Guernina and Sawyer, 2003; Bartoli, 2017). These estimates typically range from ~20–50 % total melt depending on protolith compositions and P-T-time conditions.

Discussion and Conclusions

Although our assumption of complete melt segregation may be an overestimate, significant melt loss is a common feature associated with granulite facies terranes (e.g., Brown, 2002; Guernina and Sawyer, 2003), and a minimum of 50–70 % of generated melt (assuming 40 % total melt) must be lost in order to retain a HT mineral assemblage (White and Powell, 2002). If melt is not fully lost from the system, our model requires greater total melt fractions in order to match $[\text{K}/\text{Ca}]_{\text{mdrn}}$ measured in the samples today. This suggests that our melting model (which uses minimum $[\text{K}/\text{Ca}]_{\text{protolith}}$ estimates and assumes total loss of melt), provides minimum estimates for total melt fractions.

Based on ϵ_{Ca} data, and assuming conservative protolith ages for each locality, we find that many LCC samples from the Napier Complex, Ivrea-Verbano Zone, and the Slave Province have undergone significant amounts of K depletion, with relative K/Ca decreases ranging from ~60 % to greater than 95 %. These results confirm that K, which is inferred to be the most important heat producing element in the Archean, is efficiently mobilised and removed from the lower crust during HT metamorphism. This observation implies that greater

fractions of mafic rock in the lower crust are not necessary to explain modern heat flow data, and supports crustal evolution models where continental stabilisation is promoted through HT metamorphism and depletion of radioactive elements from the lower crust.

Acknowledgements

We thank N. Botto, S. Matveev, A. Locock, W. Yang, T. Teague, and S.T. Brown for their technical expertise, C. Yakymchuk and S. Ferrero for helpful discussions, and N.J. Pester for modern hydrothermal fluid samples. This research was primarily supported by a U.S. National Science Foundation (EAR100500) grant to DJD. TC acknowledges funding from a Natural Sciences and Engineering Research Council of Canada (NSERC) discovery grant, and MAA acknowledges NSERC postgraduate funding that aided in supporting this work. ESG thanks the Australian Antarctic Division for the opportunity to participate in the 1977–1978 Australian National Antarctic Research Expedition and for logistic support, and acknowledges NSF grant DPP 76-80957 to UCLA.

Editor: Helen Williams

Author Contributions

MAA and DJD designed research; MAA performed analyses; MAA, DJD, and TC analysed data; ESG, TC, DR and DJD provided samples collected in the field; MAA and DJD wrote the paper with input from TC, DR and ESG.



Additional Information

Supplementary Information accompanies this letter at <http://www.geochemicalperspectivesletters.org/article1904>.



This work is distributed under the Creative Commons Attribution Non-Commercial No-Derivatives 4.0 License, which permits unrestricted distribution provided the original author and source are credited. The material may not be adapted (remixed, transformed or built upon) or used for commercial purposes without written permission from the author. Additional information is available at <http://www.geochemicalperspectivesletters.org/> copyright-and-permissions.

Cite this letter as: Antonelli, M.A., DePaolo, D.J., Chacko, T., Grew, E.S., Rubatto, D. (2019) Radiogenic Ca isotopes confirm post-formation K depletion of lower crust. *Geochem. Persp. Let.* 9, 43–48.

- RUDNICK, R.L., GAO, S. (2014) 4.1 – Composition of the Continental Crust. In: Holland, H., Turekian, K. (Eds.) *Treatise on Geochemistry*. Second Edition, Elsevier, Oxford, 1–51.
- RUDNICK, R.L., MCLENNAN, S.M., TAYLOR, S.R. (1985) Large ion lithophile elements in rocks from high-pressure granulite facies terrains. *Geochimica et Cosmochimica Acta* 49, 1645–1655.
- STEPANOV, A.S., HERMANN, J., KOSAKOV, A.V., RUBATTO, D. (2014) Geochemistry of ultrahigh-pressure anatexis: Fractionation of elements in the Kokchetav gneisses during melting at diamond-facies conditions. *Contributions to Mineralogy and Petrology* 167, 1–25.
- STEPANOV, A.S., HERMANN, J., RUBATTO, D., KOSAKOV, A.V., DANYUSHEVSKY, L. V. (2016) Melting history of an ultrahigh-pressure paragneiss revealed by multiphase solid inclusions in garnet, Kokchetav massif, Kazakhstan. *Journal of Petrology* 57, 1531–1554.
- WHITE, R.W., POWELL, R. (2002) Melt loss and the preservation of granulite facies mineral assemblages. *Journal of Metamorphic Geology* 20, 621–632.
- YAKYMCHUK, C., BROWN, M. (2014) Consequences of open-system melting in tectonics. *Journal of the Geological Society* 171, 21–40.

References

- ARANOVICH, L.Y., MAKHLUF, A.R., MANNING, C.E., NEWTON, R.C., TOURET, J.L.R. (2016) Fluids, Melting, Granulites and Granites: A Controversy - Reply to the Commentary of J.D. Clemens, I.S. Buick and G. Stevens. *Precambrian Research* 278, 400–404.
- BARTOLI, O. (2017) Phase equilibria modelling of residual migmatites and granulites: An evaluation of the melt-reintegration approach. *Journal of Metamorphic Geology* 35, 919–942.
- BARTOLI, O., ACOSTA-VIGIL, A., FERRERO, S., CESARE, B. (2016) Granitoid magmas preserved as melt inclusions in high-grade metamorphic rocks. *American Mineralogist* 101, 1543–1559.
- BROWN, M. (2002) Retrograde processes in migmatites and granulites revisited. *Journal of Metamorphic Geology* 20, 25–40.
- CLEMENS, J.D., BUICK, I.S., STEVENS, G. (2016) Fluids, melting, granulites and granites: A commentary. *Precambrian Research* 278, 394–399.
- DEPAOLO, D.J., MANTON, W.I., GREW, E.S., HALPERN, M. (1982) Sm–Nd, Rb–Sr and U–Th–Pb systematics of granulite facies rocks from Fyfe Hills, Enderby Land, Antarctica. *Nature* 298, 614–618.
- EWING, T.A., RUBATTO, D., HERMANN, J. (2014) Hafnium isotopes and Zr/Hf of rutile and zircon from lower crustal metapelites (Ivrea-Verbano Zone, Italy): Implications for chemical differentiation of the crust. *Earth and Planetary Science Letters* 389, 106–118.
- FERRERO, S., GODARD, G., PALMIERI, R., WUNDER, B., CESARE, B. (2018) Partial melting of ultramafic granulites from Dronning Maud Land, Antarctica: constraints from melt inclusions and thermodynamic modeling. *American Mineralogist* 103, 610–622.
- GAO, P., ZHENG, Y.F., ZHAO, Z.F. (2016) Experimental melts from crustal rocks: A lithochemical constraint on granite petrogenesis. *Lithos* 266–267, 133–157.
- GREEN, E.C.R., WHITE, R.W., DIENER, J.F.A., POWELL, R., HOLLAND, T.J.B., PALIN, R.M. (2016) Activity–composition relations for the calculation of partial melting equilibria in metabasic rocks. *Journal of Metamorphic Geology* 34, 845–869.
- GUERNINA, S., SAWYER, E.W. (2003) Large-scale melt-depletion in granulite terranes: An example from the Archean Ashuanipi subprovince of Quebec. *Journal of Metamorphic Geology* 21, 181–201.
- HACKER, B.R., KELEMEN, P.B., BEHN, M.D. (2015) Continental Lower Crust. *Annual Review of Earth and Planetary Sciences* 43, 167–205.
- KELSEY, D.E., HAND, M. (2015) On ultrahigh temperature crustal metamorphism: Phase equilibria, trace element thermometry, bulk composition, heat sources, timescales and tectonic settings. *Geoscience Frontiers* 6, 311–356.
- MARSHALL, B.D., DEPAOLO, D.J. (1989) Calcium isotopes in igneous rocks and the origin of granite. *Geochimica et Cosmochimica Acta* 53, 917–922.
- PALIN, R.M., WHITE, R.W., GREEN, E.C.R. (2016) Partial melting of metabasic rocks and the generation of tonalitic-trondhjemite-granodioritic (TTG) crust in the Archaean: Constraints from phase equilibrium modelling. *Precambrian Research* 287, 73–90.
- REDLER, C., JOHNSON, T.E., WHITE, R.W., KUNZ, B.E. (2012) Phase equilibrium constraints on a deep crustal metamorphic field gradient: Metapelitic rocks from the Ivrea Zone (NW Italy). *Journal of Metamorphic Geology* 30, 235–254.



Radiogenic Ca isotopes confirm post-formation K depletion of lower crust

M.A. Antonelli, D.J. DePaolo, T. Chacko, E.S. Grew, D. Rubatto

Supplementary Information

The Supplementary Information includes:

- 1. Sample descriptions and Petrography
- 2. Methods
- Tables S-1 to S-6
- Figures S-1 to S-6
- Supplementary Information References

1. Sample Descriptions and Petrography

Granulite-facies metamorphism occurs when rocks are subjected to temperatures greater than about 800 °C. This condition of prolonged high temperature can occur in geologic settings ranging from short-duration heating events (<20 Myr) in back-arc settings (Brown, 2006, 2007; Pownall *et al.*, 2014), to regional-scale long-duration events (up to 100 Myr) in large hot orogenies (LHO) (Harley, 2016; Kelsey and Hand, 2015), as well as during rifting and extreme subduction of crust (Hermann and Rubatto, 2014). Details of past metamorphic settings are inferred using a combination of geochronology, thermobarometry, and pseudosection modeling, and mainly differ based on pressure-temperature-time (P-T-t) paths, which range from clockwise heating/pressurisation with subsequent decompression (gradual to near isothermal) to heating followed by near isobaric cooling at depth (Harley, 2016).

Twelve ultrahigh-temperature (UHT) granulite samples were collected by E.S.G. in January 1978 on an east-west traverse of Dallwitz Nunatak, in the Archean Napier Complex (NC), Enderby Land, East Antarctica. Four lower crustal granulite xenoliths, provided by T.C., come from the Diavik Diamond Mine in the Lac-de-Gras region of Canada (Slave Province, SP). One ultrahigh-temperature (UHT) facies metapelite, along with two mafic amphibolites, come from the Ivrea-Verbano Zone (IVZ), collected by D.R. along a transect of increasing temperature. A fourth sample (IV-16-19) is determined to be a late-stage crustally-contaminated gabbro intrusion in the same area. A single sample of the Sumdo eclogite (SE) was collected by D.J.D. from the Lhasa Block, Tibet. The P-T-t paths for the three major locations vary from short-lived clockwise heating (up to UHT conditions) and exhumation in the IVZ (Ewing *et al.*, 2013; Pape *et al.*, 2016; Redler *et al.*, 2012) with peak pressures up to ~1.2 GPa, to long-lived heating followed by isobaric cooling in the NC and SP at pressures ~1.0–1.3 GPa (Davis *et al.*, 2003; Harley, 2016; Mitchell and Harley, 2017, this study).

1.1. Antarctic Samples (Napier Complex)

The NC exposed in Dallwitz Nunatak (formerly called Spot 945, which has coordinates 66° 57' S, 51° 30' E and is part of the Tula Mountains east of Amundsen Bay, Enderby Land) comprises a variety of rock types metamorphosed under UHT conditions, including mafic and pelitic granulites and subordinate migmatite units and granitic gneisses. Samples are numbered increasing from west to east, with samples 2033 and above collected northeast of the summit. According to PT estimates for the region, our samples



are likely to have formed at ~1.0 GPa with peak temperatures of ~900 °C, followed by slow isobaric cooling (Harley, 2016; Mitchell and Harley, 2017). We describe the mineralogy and field relationships as follows:

2030B. Mafic layer in a pyroxene-plagioclase granulite. Dominantly orthopyroxene with minor plagioclase and clinopyroxene; granoblastic texture. Traces of secondary biotite. Opx and Cpx show lamellar exsolution, plagioclase has traces of antiperthitic exsolution.

2032A. Layered garnet-sapphirine-quartz metapelite, interbedded with mafic pyroxene granulite (2032I). Sapphirine grains are free of garnet inclusions. Sapphirine is overgrown by garnet, sillimanite, and cordierite. Hercynite and quartz are included in the sapphirine. Cordierite displays twinning; vermicular cordierite-quartz symplectites are fairly abundant. Rare orthopyroxene grains and secondary biotite are also present.

2032I. Equigranular mafic pyroxene granulite alternating with layers of metapelite (2032A). Dominantly orthopyroxene with minor plagioclase and clinopyroxene. Both clinopyroxene and orthopyroxene have lamellar structure. Minor secondary biotite.

2033A. Coarse-grained mafic pyroxene granulite. Dominantly plagioclase with subordinate orthopyroxene and clinopyroxene, granoblastic texture. Secondary olive-colored hornblende and biotite replacing pyroxenes also present. Minor antiperthitic exsolution.

2035A. Center of metamorphosed ultramafic dike. A coarse-grained biotite-pyroxene mafic rock showing lineation and foliation with dominant orthopyroxene, subordinate plagioclase, olivine, clinopyroxene & hornblende, and minor biotite with indistinct preferred orientation. Olivine appears relatively fresh. Pyroxenes exhibit lamellar exsolution. Minor hercynite and opaques (prob. magnetite) are intergrown. The dike is 1.7 m thick with a paler marginal zone 7-8 cm thick (2035B) and pinches out to the east. The lower contact is folded, and appears to be discordant, possibly because of transposition. Overall, the dike appears concordant with the gneissic layering.

2035B. Outer-edge of metamorphosed ultramafic dike. From pale-colored, 7-8 cm thick, marginal zone of mafic dike (2035A). Strong granoblastic texture, dominantly orthopyroxene with minor plagioclase and clinopyroxene. Minor hornblende and biotite are included within orthopyroxene, which has a lamellar structure. Plagioclase shows minor antiperthitic exsolution.

2036A. Rusty garnet quartzite unit, finely layered white and gray on centimeter scale. Interbedded with units represented by samples 2036C and 2036E. Dominated by quartz-cordierite vermicular intergrowths, subordinate garnet, K-feldspar, and well-aligned sillimanite. Minor euhedral sillimanite, rutile, and hercynite inclusions in garnet. Hercynite grains appear entrained in quartz-cordierite-K-feldspar regions (interpreted as trapped melt). K-feldspar contains minor perthitic exsolution.

2036C. Fine-grained, rusty garnet-sillimanite quartzite with melt veinlets. Dominantly quartz and cordierite with strongly perthitic K-feldspar (interpreted to be trapped melt) with significant amounts of garnet and sillimanite.

2036E. Coarse-grained, garnet-sillimanite quartzite. Dominantly garnet with subordinate quartz and plagioclase. Plagioclase has minor antiperthitic exsolution. Hercynite is included in garnet. Minor secondary biotite around garnet. Sillimanite lineation seems to be parallel to measured fold axes of the outcrop layers, also outlined by garnet and possible orthopyroxene.

2038. Leucocratic aplitic gneiss from migmatite unit. Dominantly quartz, K-feldspar with string perthite exsolution, and minor rutile garnet and subordinate sillimanite. Garnet has inclusions of K-feldspar and quartz, along with minor amounts of ilmenite, rutile, monazite & zircon.

2040C. Garnet-pyroxene-biotite lens (about 1m across in a mafic layer). Dominantly garnet and orthopyroxene, minor quartz and traces of secondary biotite rimming garnet. Granoblastic texture. Garnet has abundant rounded quartz inclusions. There is a single patch of possible cordierite + quartz "fingerprint" symplectite.

2044. Granitic gneiss collected from eastern-most part of outcrop. Dominantly K-feldspar with subordinate quartz and minor plagioclase and orthopyroxene with traces of skeletal garnet and secondary biotite. Feldspar is mesoperthitic, but locally grain margins free of lamellae, opaques have inclusions of spinel (hercynite). Minor alteration of Opx.

1.2. Diavik Xenolith Samples (Slave Craton)

The four xenoliths in this study are from the A154N kimberlite pipe, Diavik Diamond Mine, NT, Canada. They represent pieces of the lower crust that have been transported to the surface much faster than those in high-grade terranes such as NC and IVZ. As a result of the emplacement processes, we do not have spatial information for the xenolith samples, which are likely to be from variable depths in the lower crust. We constrain their metamorphic conditions using traditional geothermobarometric techniques (TWEQU software package) and microprobe data collected at the University of Alberta (Table S-3) and find that they generally come from crustal depths of approximately 35-45 km (1.0-1.3 GPa), have uniform garnet compositions along transects, and yield (minimum) peak metamorphic temperatures between 760-870 °C. Although younger metamorphic events have been recorded in the Slave Province (Aulbach *et al.*, 2010; Davis *et al.*, 2003), two samples (including one that was not analysed in this study, DDM20) have LA-



ICP-MS metamorphic zircon Pb-Pb ages ranging from ~2.53 to ~2.58 Ga (analysed at the University of Alberta) and our Fe-Mg exchange temperature-estimates (described for each sample) suggest that the samples were not reset after the major episode of granulite metamorphism in the Slave province *ca.* 2.5 Ga (Davis *et al.*, 2003). The mineralogy and PT estimates are as follows:

DDM163. Coarse-grained mafic granulite. Dominantly clinopyroxene, clean labradoritic plagioclase, and euhedral garnet, with minor orthopyroxene exhibiting a generally granoblastic texture. Traces of hornblende rimming opaques (FeS_x) and rutile. Orthopyroxenes have lamellar structure. Garnet-clinopyroxene and garnet-orthopyroxene Fe-Mg exchange thermometry indicate temperatures of 760-840 °C. Given the susceptibility of Fe-Mg exchange thermometers to re-equilibration on slow cooling of granulite-facies rocks (e.g. Frost and Chacko, 1989), these temperatures should be regarded as minimum estimates of the peak metamorphic temperature experienced by this sample. Garnet-plagioclase-pyroxene-(quartz) barometry suggests maximum pressures of 1.1-1.3 GPa.

DDM303. Kyanite-garnet-plagioclase metapelitic xenolith. Dominantly plagioclase and rutile garnet, with abundant opaque grains of at least two varieties. Black-colored opaques surround garnets. Subordinate K-feldspar, orthopyroxene, and kyanite, along with veins of serpentine and chlorite which may have intruded from the kimberlite. K-feldspar is perthitic. Minerals in smaller proportions include rutile, secondary biotite (around opaque minerals), apatite, hercynite, monazite, zircon, magnetite, ilmenite, and pyrite. Garnet-orthopyroxene-plagioclase-(quartz) thermobarometry indicate a minimum temperature of 770 °C and maximum pressures of ~1.2 GPa (using kyanite reactions the pressure estimate is slightly higher, ~1.3 GPa). Two ~150 µm metamorphic zircon grains (containing inclusions of garnet) yielded a $^{207}\text{Pb}/^{206}\text{Pb}$ age of 2528 ± 8.6 Ma ($n = 7$) by LA-ICP-MS at the University of Alberta.

DDM309. Coarse-grained equigranular mafic xenolith. Composed of clean clinopyroxene, plagioclase, and euhedral garnet, along with minor amounts of clean orthopyroxene. Plagioclase shows very strong labradorite-like texture. Pyrite and apatite are also present. Small amounts of secondary hornblende around mafic minerals. Strong granoblastic texture, no kimberlite intrusion appears to be present. Garnet-orthopyroxene and garnet-clinopyroxene Fe-Mg exchange thermometry yields minimum temperature estimates of 840-880 °C with garnet-plagioclase-pyroxene-(quartz) maximum pressures of 1.0 – 1.1 GPa.

DDM342. Coarse-grained anorthositic mafic xenolith. Composed dominantly (~80%) of very clean plagioclase separating subordinate garnet and small amounts of clinopyroxene, generally found in association with each other. Abundant string-perthite exsolution also present. Rutile garnets and clinopyroxene grains appear slightly resorbed at margins. Celsian and chlorite present along fractures. Clinopyroxene rimmed by chlorite then celsian, potentially from kimberlite intrusion. Garnet-clinopyroxene-plagioclase-(quartz) thermobarometry gives a minimum temperature of 870 °C and maximum pressure of 1.3 GPa.

1.3. Ivrea-Verbano Samples

The Ivrea-Verbano Zone contains packages of mafic and pelitic rocks that gradually increase in metamorphic grade from amphibolite to upper granulite/UHT facies (Redler *et al.*, 2012). Four samples from Ivrea were collected by D.R. during the field season of 2016, along the main road in the Strona Valley. We have analysed lower-temperature (amphibolite) mafic rocks from one end of the sequence (~700 °C), a UHT facies metapelitic from the other end of the sequence (> 870 °C), and a crustally-contaminated garnet-bearing mafic intrusion (which is not thought to have lost melt and is included only for reference in Fig. 1). Pressure and temperature conditions for samples that are part of the sequence can be deduced based on their locations compared to published isobars (0.6-1.0 GPa) and isotherms for the region, for which there is an inferred clockwise P-T-t path (Redler *et al.*, 2012).

IV-16-09. A banded quartz-biotite-plagioclase schist with garnet porphyroblasts and minor sillimanite, chlorite, apatite, and K-feldspar. Main garnets contain inclusions of rounded quartz, FeS, and ilmenite. A small population of rare fine-grained REE-enriched garnets were also identified in a corner of the sample. The sample is from the low temperature part of the sequence when large garnet first appear in the metapelites (45°54'54" N, 08°13'35" E), past the K-feldspar (+ sillimanite)-in isograd (Redler *et al.*, 2012). Temperature is estimated to be ~700-750 °C with pressures of ~0.6-0.9 GPa.

IV-16-19. Garnet-plagioclase amphibolite. Dominantly composed of hornblende with subordinate garnet and plagioclase. Garnet is highly fractured and rounded suggesting extensive post-crystallisation deformation. Ilmenite grains are associated with hornblende and garnet. Plagioclase is strongly altered, possibly to microcrystalline epidote. Hornblende + quartz symplectites rim garnet. This sample is from the main lower crustal gabbro, with abundant crustal contamination (thus the garnet), which outcrops in the upper part of the valley at Campello Monti (45°56'05" N, 08°14'16" E). The contact between gabbro and the UHT metapelites is not exposed along the Val Strona road. Large-scale mapping suggests that the gabbro cross-cuts the regional UHT metamorphism. A better studied section in Val Sesia has a highly contaminated gabbro which probably intruded at 0.5-0.7 GPa (we are not aware of any direct estimate of P in the Campello mafic body). The original temperature of crystallisation was likely around 1000-1200 °C (solidus for a gabbro), but because the gabbro was intruded into the hot lower crust, it is expected that it slowly cooled to amphibolite-facies. Many of the lower crustal gabbros in Ivrea are amphibole bearing, yet whether or not the amphibole itself is a primary product remains an open question.



IV-16-24. Garnet-K-feldspar-quartz metapelite. Dominated by K-feldspar and garnet, with subordinate quartz, cordierite, and sillimanite. Fairly abundant opaques (mostly ilmenite). K-feldspar is perthitic. Sillimanite, quartz, rutile, ilmenite, and minor monazite inclusions in garnet. Ilmenite found partially replacing rutile; cordierite-quartz symplectites replacing garnets. The sample is from the high temperature section of Val Mastallone ($45^{\circ}52'51''$ N, $08^{\circ}10'21''$ E), where slivers of metapelites (septa) are found within the main gabbro body. Peak temperatures determined by thermodynamic modeling are > 870 °C and pressures > 0.95 GPa (Redler *et al.*, 2012). Zr-in-rutile thermometry for the Val Mastallone septa indicates extreme T of 1020–1050 °C (Ewing *et al.*, 2013; Pape *et al.*, 2016).

IZ-408(L&M). A banded amphibolite grade mafic rock displaying incipient melting, containing mainly amphibole and plagioclase. The ground mass is dominantly composed of equigranular hornblende showing weak preferred orientation, interspersed with quartz and plagioclase, and containing minor amounts of ilmenite, titanite (from ilmenite), muscovite, apatite, & magnetite. Quartz, epidote, and more albitic plagioclase are concentrated in the leucosomes along with traces of zircon, chalcopyrite, and calcite. A quartz-rich leucosome (IZ-408L) and typical melanosome ground-mass (IZ-408M) were separated for individual XRF and Ca-isotope analyses. The sample was collected from one of the large bodies of amphibolite within the metapelites and the locality is in between the K-feldspar-in and the biotite-out isograds (for the metapelites) near the locality of Rosarolo (temperatures ~ 800 °C at ~ 0.8 GPa) (Redler *et al.*, 2012).

1.4. Sumdo Eclogite

The single eclogite sample analysed in this study was collected in 2014 by D.J.D. from the Sumdo Group, Lhasa Block, Tibet, at a location of $29^{\circ}52'22.9''$ N, $92^{\circ}31'33.5''$ E, near the town of Xianduogang, Gongbo'gyamda, Nyingchi. The sample is of Permian age (~ 275 Ma) from U-Pb dating of zircons (Weller *et al.*, 2016; Yang *et al.*, 2009).

14DLB39. Coarse-grained mafic eclogite. Dominantly composed of omphacite and garnet with subordinate quartz and minor yet significant amounts of large rutile and large rounded apatite grains (in equal abundance). Garnet is highly fractured and appears partially replaced by clinopyroxene with higher aegirine component than the main omphacite. Rutile is associated with garnet and also found as inclusions in garnet. Minor zircon inclusions also in garnet. PT estimates based on previous work suggest relatively high-T (~ 700 °C) and pressures of ~ 2.7 GPa (Weller *et al.*, 2016; Yang *et al.*, 2009).

2. Methods

We characterised the modal mineralogy (Table S-1), bulk-rock chemical composition (Table S-2), in-situ mineral compositions (Table S-3), and mineral-separate compositions (Table S-4) for each sample through optical and chemical image analysis methods, x-ray fluorescence (XRF) spectroscopy, electron probe micro-analysis (EPMA), inductively-coupled plasma optical-emission spectroscopy (ICP-OES) & isotope dilution thermal-ionisation mass spectrometry (ID-TIMS), respectively. A ^{42}Ca - ^{48}Ca double-spike method was used to determine $[^{44}\text{Ca}]$ for the mineral separates used in isochron age calculations (Table S-4). Unspiked calcium separates were measured for their Ca isotopic composition by TIMS at the University of California, Berkeley.

2.1. Analytical Methods

Modal Mineralogy. Estimates were obtained through optical microscopy, combined with image analysis methods (using back-scattered electron maps and optical scans). BSE maps and thin-section X-ray maps (Fe, Mg, Si, Al, Ca) were used instead of optical scans for the SP xenoliths. All of the BSE maps were obtained using a 15 kV, 10 nA beam, with a fully-focused spot. The results of the modal mineral estimates are reported in Table S-1.

Whole-Rock Compositions. For the NC samples, whole-rock chemistry was determined by X-Ray Fluorescence (XRF) at the University of California, Berkeley, using ~ 10 g aliquots of powdered bulk-rock prepared in a steel disk-mill, homogenised, and fused into disks. The IVZ and SE samples were sent to the Geoanalytical Laboratory at Washington State University (WSU), along with one SP xenolith (DDM309). For the majority of SP samples, whole-rock chemistry was reconstructed based on combining modal mineralogy with major mineral compositions. The reconstructed whole rock chemistry of DDM309 was compared to the XRF values. We found that intrusion of kimberlitic magma into the xenolith leads to a significantly higher Mg# than that derived from reconstructed whole-rock chemistry, but the K and Ca concentrations and K/Ca ratio are approximately the same; nevertheless, we use the reconstructed values for the SP samples in the figures and text. The whole-rock compositions, along with Mg#, A/CNK, and K/Ca values, are reported in Table S-2.

In-Situ Mineral Compositions. Mineral compositions were obtained using EPMA at the University of California, Davis (NC, IVZ,



and SE samples) and at the University of Alberta (SP samples). Quantitative analyses were generally run at 15 kV (10 nA) with a 1- μm spot size, except for plagioclase which had a 10- μm spot size. The results of the microprobe analyses for garnet, plagioclase, and K-Feldspar, along with their calculated solid-solution compositions, are reported in Tables S-3.

Mineral-Separate Compositions. Garnet and feldspar separates were obtained through manual mineral separation of whole-rocks crushed in a tungsten carbide impact-mortar and immersed in isopropyl alcohol. Fine tweezers, stereoscopic microscope, and both black and white weighing trays were used in order to select clean grains, which were subsequently dissolved in acid for the various analyses (following section). The various mineral separates ranged from ~10 to ~100 mg. Given availability, aliquots of the dissolved mineral separates and whole-rock powders were analysed for Mg, Ca, Na, and K concentrations by ICP-OES at the University of California, Berkeley. For our isochron determinations, we analysed mineral separates and whole rocks for their K and Ca concentrations by ID-TIMS, using a combined ^{41}K - ^{43}Ca spike and calibrating to four USGS standards (AGV-2, DNC-1, GSP-2, & W2-A). Measurements of molar ^{44}Ca concentration for all of the isochron-related samples were performed using a ^{42}Ca - ^{48}Ca double-spike technique generally used for measuring $\delta^{44}\text{Ca}$ at UC-Berkeley. This corrects for possible stable isotope fractionation in the samples. The purity of our dissolved mineral separates was verified by comparing the above analyses to those measured in-situ by EPMA. The results are reported in Table S-4.

Ca-Isotope Analyses. For ε_{Ca} analysis, ~10–100 mg of sample is weighed in screw-top Savillex beakers and dissolved using a 5:2:1 combination of concentrated hydrofluoric, 6N hydrochloric, and concentrated perchloric acid. After a minimum digestion period of one week at 130 °C, the samples are evaporated to dryness under flowing-N₂ in pot-stills. The dry samples are then redissolved in 3N nitric acid, from which aliquots are taken for the various TIMS and ICP-OES analyses. Difficulty dissolving certain samples is overcome by (i) dissolving fluorides in 6N hydrochloric acid, (ii) repeating the initial dissolution, and in extreme cases, (iii) placing the beakers in a heated ultrasonic bath (~60 °C) for extended periods of time.

Calcium is separated using established column-chemistry methods (Eichron DGA resin, Simon *et al.*, 2009) and several standards (USGS dolerites DNC-1 and W2a, and Ca isotope standard SRM915a) are run alongside the samples. After washing away matrix elements with 3N nitric acid, purified calcium is collected in acid-refluxed Savillex beakers using ultrapure water. The water is evaporated, and remaining solid is treated with a drop of concentrated nitric acid and 30% hydrogen peroxide, for a period of > 24 hours, in order to dissolve resin that may have come through the column. After the acid is evaporated, 3–5 μg of Ca is loaded onto out-gassed rhenium filaments in ~1 μL of 3M nitric and dried down. The dried aliquot is covered with ~1 μL of 40% phosphoric acid and heated on the filament for increased sample stability. Full coverage of the filament with phosphoric acid (as opposed to separate domains connected by stringers) is found to yield more consistent results, and a stereoscopic microscope is used to ensure enough H₃PO₄ is added to each filament.

The filaments are loaded into a ThermoFisher Scientific Triton TIMS analyzing ^{40}Ca , ^{42}Ca , ^{43}Ca , and ^{44}Ca . We use a double-filament method that takes ~3 hours per analysis. Current is slowly increased through the evaporation filament at 50 mA/min and through the ionisation filament at 120 mA/min (up to a combined temperature of ~1410 C, ~3000 mA for most ionisation filaments). When the evaporation filament reaches 1600 mA, the current is increased more slowly to ~1800 mA (at 10 mA/min) and the amplifier gains are re-calibrated during this period. Afterwards, we focus the beams and slowly increase current through the evaporation filament until there is ~18 volts for ^{40}Ca (typically at 1850–2200 mA). Peak-scans are performed prior to starting each measurement, which we use to correct for subtle changes in beam-alignment that can sometimes occur between samples. Generally, the ^{40}Ca signal slowly grows to ~25 V by the end of the acquisition, which consists of 10 blocks of 20 lines. Each line acquires Ca isotope data for ~10 seconds and ^{39}K data for ~1 second (always < 1 ppm compared to ^{40}Ca) and is followed by ~4 seconds of downtime. Each block is separated by an automated peak-centering and lens-focusing cycle.

2.2. Bulk Silicate Earth (BSE) $^{40}\text{Ca}/^{44}\text{Ca}$ and ε_{Ca} Uncertainty

We infer BSE to have $^{40}\text{Ca}/^{44}\text{Ca} = 47.156 \pm 0.001$ (2SE, n = 24) (at a corresponding $^{42}\text{Ca}/^{44}\text{Ca} = 0.31221$), which is in accordance with our analyses of USGS dolerite standards W2a and DNC-1, modern hydrothermal vent fluids from Lost-City, and several mafic granulites from this study (Table S-5). Other measurements of mafic-to-intermediate igneous rock standards (He *et al.*, 2016; Mills *et al.*, 2018; Schiller *et al.*, 2012), and enstatite chondrites (Simon *et al.*, 2009) corroborate this value, which is about ~1 epsilon unit lower than calcium isotope standard SRM915a [$^{40}\text{Ca}/^{44}\text{Ca} = 47.163 \pm 0.002$ (2SE, n = 18), this study]. Our values of $^{40}\text{Ca}/^{44}\text{Ca}$ and $^{42}\text{Ca}/^{44}\text{Ca}$, yield a value for $^{40}\text{Ca}/^{42}\text{Ca}$ of 151.039 ± 0.006 which compares favorably to the previously proposed value (Marshall and DePaolo, 1982) of 151.024 ± 0.016 .

We have been able to distinguish the subtle differences in standard compositions through large numbers (n > ~10) of carefully repeated analyses, however, this is impractical for a large number of samples. We find that repeating a measurement twice provides adequate accuracy. The average difference between replicate ε_{Ca} analyses in this study (35 samples, excluding the standards) is ~0.8, which is skewed by a small number of samples with poor reproducibility (excluding five outliers, the average is ~0.6).



However, due to drift in the machine over time, gradual cup passivation, and other sources of variability, we report a more-conservative uncertainty of ± 1 for ε_{Ca} in our figures and tables.

2.3. K-Ca Isochrons

High-K whole rocks and feldspar separates, which were analysed in order to build ^{40}K - ^{40}Ca isochrons, have ε_{Ca} ranging from +4 to +75, with higher values generally found in older samples with higher K/Ca ratios (Figure S-1). Incorporating [Ca] and [^{44}Ca] from double-spiked TIMS analyses and [K] from ID-TIMS or ICP-OES analyses (see Table S-4a,b), our measurements yield ages of 2.6 to 2.0 Ga (± 0.2 Ga, 2SD) with an average of 2.3 Ga for the NC ($n = 4$) and 0.4 ± 0.4 Ga (2SD) for the IVZ ($n = 1$) (Figure S-2).

Although the isochrons have a maximum of three-points and are not reliable for accurate age determinations, the ages they provide are in general agreement with more precise dating methods for the Northern NC (~2.5 Ga) (Harley, 2016; Horie *et al.*, 2012) suggesting closed-system evolution of ^{40}K - ^{40}Ca in our samples after metamorphism. Oxygen isotope thermometry from the same region of the NC as our study (Farquhar *et al.*, 1996) has also shown that garnet is particularly resistant to retrograde exchange, even during protracted reheating and deformation. Although metamorphic ages in the IVZ (~0.3 Ga) are in agreement with our results (Redler *et al.*, 2012), our uncertainties are too large to rule out post-metamorphic K-Ca redistribution. The SP xenoliths and Sumdo eclogite were not used for K-Ca dating due to low whole-rock K/Ca values and possible effects of kimberlite-related metasomatism in the bulk xenoliths.

2.4. Protolith K/Ca Calculations

The Antarctic samples in our study (NC) were collected from Dallwitz Nunatak, which has Sm-Nd and inherited zircon protolith ages up to ~3.5 Ga (DePaolo *et al.*, 1982; Horie *et al.*, 2012; Kelly and Harley, 2005; Kusiak *et al.*, 2013) and a metamorphic age of ~2.5 Ga (Harley, 2016; Horie *et al.*, 2012). Available data for lower crustal xenolith samples from the Slave province (from the same kimberlite as our samples) have Re-Os model ages ranging up to ~3.3 Ga (Aulbach *et al.*, 2010) but most lower-crustal xenoliths have ~2.6 Ga protolith ages (Davis *et al.*, 2003; Pehrsson *et al.*, 2000). We use a conservative estimate of 3.0 Ga for our calculations. Metamorphic ages for the SP are also generally ~2.5 Ga (Davis *et al.*, 2003). For the IVZ, Sm-Nd protolith ages range up to ~0.6 Ga (Voshage *et al.*, 1987), and the oldest detrital zircon ages in metapelites range up to ~550 Ma, with numerous samples around 450 Ma (Kunz *et al.*, 2018). We use a protolith age of 0.6 Ga to remain conservative in our K/Ca calculations. The IVZ metamorphic ages cluster around ~0.3 Ga (Ewing *et al.*, 2013; Kunz *et al.*, 2018; Vavra *et al.*, 1996). The single sample from Tibet (SE) has a U-Pb zircon age of 0.27 Ga (Weller *et al.*, 2016), but does not have garnet ε_{Ca} resolvable from BSE or available protolith age estimates. In our use of Equation 1 from the main text, we chose the oldest protolith age from each locality in order to generate minimum estimates for protolith K/Ca, but have not incorporated uncertainties in the protolith ages themselves.

The expression for calculating $[\text{K}/\text{Ca}]_{\text{protolith}}$, given ε_{Ca} values and protolith/metamorphic ages [equation (2) in the main text], incorporates the factor Q_{Ca} , modified from (Marshall and DePaolo, 1989). In our formulation, Q_{Ca} is equal to ~1.0804 defined:

$$Q_{\text{Ca}} = \frac{R_{\beta} [{}^{40}\text{K}(ab)/{}^{44}\text{Ca}(ab)] \cdot 10000}{({}^{40}\text{Ca}/{}^{44}\text{Ca})_{\text{BSE}}} \quad (\text{Eq. S-1})$$

Where R_{β} is the branching ratio for ^{40}K decay [$\lambda_{\beta}/(\lambda_{\beta}+\lambda_{\text{EC}})$, equal to 0.8952], ${}^{40}\text{K}(ab)$ is the modern isotopic abundance of ^{40}K relative to total K (0.000117) and ${}^{44}\text{Ca}(ab)$ is the isotopic abundance of ^{44}Ca relative to total Ca [equal to 0.020558, assuming $({}^{40}\text{Ca}/{}^{44}\text{Ca})_{\text{BSE}}$ is 47.156].

In order to calculate $[\text{K}/\text{Ca}]_{\text{protolith}}$ for samples where garnet was not available, we used low K/Ca plagioclase separates (verified by ICP-OES) to constrain initial ε_{Ca} . For sample 2044, we used whole rock K/Ca values and assumed an age of 2.5 ± 0.3 Ga in order to estimate initial ε_{Ca} . For sample IZ-408M and 2035A, the measured whole-rock K/Ca is low enough to assume ε_{Ca} is the same today as at the time of metamorphism (Tables S-2 and S-5). Although we analysed garnet from IVZ sample IV-16-09 and SE sample 14DLB39, we excluded them from our models because the former is inferred to represent a crustally-contaminated gabbro intrusion into the IVZ and the latter is an eclogite (see sample descriptions).

2.5. Partial-melting model

In order to estimate melt-loss from our data, it is essential to constrain $[\text{K}/\text{Ca}]_{\text{melt}}$. The simplest approach for estimating $[\text{K}/\text{Ca}]_{\text{melt}}$ would be to assume that it is the same as for local granitic/migmatite samples (2038 & 2044, See Table S-2), however, the modern [K/Ca] ratios of these two samples (which were probably generated at similar conditions) are quite different. Assuming similar ages, our ε_{Ca} measurements indicate that the two migmatites were likely derived from pre-cursor materials with very different $[\text{K}/\text{Ca}]_{\text{protolith}}$



(see Fig. 3). The initial ϵ_{Ca} of migmatite 2038 (measured in garnet) is ~ 14 , whereas the initial ϵ_{Ca} of sample 2044 (calculated from whole-rock ϵ_{Ca} and $[\text{K}/\text{Ca}]_{\text{modern}}$, assuming an age of 2.5 ± 0.3 Ga) is only ~ 3 . This suggests that migmatite 2038 came from melting of a high K/Ca pelitic protolith (similar to those of 2036A, 2036C, & 2040C), whereas 2044 came from melting of a lower K/Ca igneous protolith (similar to those of our meta-granitic/mafic samples). Therefore, it appears that $[\text{K}/\text{Ca}]_{\text{protolith}}$ exerts a strong control on $[\text{K}/\text{Ca}]_{\text{melt}}$, so assuming a single melt composition would not be realistic.

We therefore construct a non-modal batch melting model, where the distribution coefficients for K and Ca are a function of the weight fractions for their residual host minerals. For a standard batch melting model, the enrichment or depletion of an element in the liquid relative to the original solid is given by:

$$\frac{C_l}{C_o} = \frac{1}{D_i(1-F)+F} \quad (\text{Eq. S-2})$$

Where F is the melt fraction, C_l is the concentration of element i in the liquid, and C_o is the concentration of element i in the original rock. We assume that the bulk distribution coefficient for K is proportional to the modal abundance of K-feldspar, and hence decreases as K-feldspar is consumed (non-modal batch melting), until there is no K-feldspar left in the solid phase.

$$\bar{D}_K(F) = \begin{cases} K_d^{K\text{spar}} \left[\frac{X_o^{K\text{spar}} - F\theta_{K\text{spar}}}{(1-F)} \right] & \text{if } \left[\frac{X_o^{K\text{spar}} - F\theta_{K\text{spar}}}{(1-F)} \right] > 0 \\ 0.0005 & \text{if } \left[\frac{X_o^{K\text{spar}} - F\theta_{K\text{spar}}}{(1-F)} \right] \leq 0 \end{cases} \quad (\text{Eq. S-3})$$

Where $K_d(\text{kspar})$ is the distribution coefficient for K-feldspar, $X_o(\text{kspar})$ is the original weight fraction of K-feldspar in the rock, and $\theta_{K\text{spar}}$ is the fraction of K-feldspar component in the generated melt. We calculate the weight fraction of K-feldspar using $[\text{K}_2\text{O}]/13.5$ (wt%) (assuming a composition of Or80), and assume a K-feldspar-absent bulk D_K of 0.0005. The incorporation of biotite as another K source in the starting materials does not greatly affect our results given the similar K concentrations and distribution coefficients for the two minerals.

Similarly for calcium, but without the possibility of total exhaustion, we have:

$$\bar{D}_{\text{Ca}}(F) = K_d^{\text{Plag}} \frac{(X_o^{\text{Plag}} - F\theta_{\text{Plag}})}{(1-F)} + K_d^{\text{Cpx}} \frac{(X_o^{\text{Cpx}} - F\theta_{\text{Cpx}})}{(1-F)} \quad (\text{Eq. S-4})$$

Where $K_d(\text{plag})$ and $K_d(\text{cpx})$ are the distribution coefficients for Ca in plagioclase and clinopyroxene, $X_o(\text{plag})$ and $X_o(\text{cpx})$ are the total weight percent of plagioclase and clinopyroxene in the rock, and θ_{Plag} and θ_{Cpx} are the fraction of plagioclase and clinopyroxene in the generated melt. Because they have similar distribution coefficients, we assume that plagioclase and clinopyroxene are present in equal abundance, and calculate their weight fractions as $[\text{CaO}]/15.8$ (wt%) (corresponding to fractions of 50% An70 + 50% Di70). The incorporation of amphibole as another Ca source in our models does not lead to significant differences in our results, given the assumptions inherent to our estimates of modal mineralogy and distribution coefficients.

A large database exists for melt-inclusions found in granulites (Bartoli *et al.*, 2016), but information linking them to their host-rock compositions is not available, making distribution coefficients hard to determine from natural data. We use a compilation of anhydrous melting experiments at 900 ± 50 C and at 1.0 ± 0.2 GPa, isolated from a larger compilation (Gao *et al.*, 2016) based on a wide variety of starting materials $[(\text{K}/\text{Ca})_{\text{protolith}}]$ ranging from ~ 0.4 to ~ 31 (Table S-6)]. Assuming a melt fraction (F) of ~ 0.2 to ~ 0.4 for the experiments at relevant PT conditions, $K_d(K)$ for K-feldspar is about ~ 4 and $K_d(\text{Ca})$ for plagioclase & clinopyroxene is also ~ 4 . Varying the K_d 's over likely ranges only slightly modifies our main results (Fig. S-6a-h), which depend most significantly on $[\text{K}/\text{Ca}]_{\text{protolith}}$.

To estimate the amount of K-feldspar and plagioclase in average granulite melts ($\theta_{K\text{spar}}$ and θ_{plag}), we use a compilation of ~ 600 melt-inclusion analyses from a wide range of granulite-facies rocks (Bartoli *et al.*, 2016). From this compilation, the average orthoclase fraction in the melt is approx. ~ 0.28 and the average anorthite fraction is ~ 0.02 . Assuming that these components are sourced from K-feldspar and plagioclase melting, this translates into 35% K-feldspar ($\theta_{K\text{spar}}$ equals 0.35, assuming Or80) and $\sim 2\%$ plagioclase ($\theta_{\text{plag}} = \sim 0.02$, assuming An70). In accordance with common Ab-An-Di phase diagrams, we set θ_{Cpx} to $\frac{1}{2}$ of θ_{plag} (~ 0.01), however, we note that at high melt fractions, when nothing but clinopyroxene and plagioclase are left in the residue, $\theta_{\text{plag}} + \theta_{\text{Cpx}}$ must equal 1. This condition, however, is not reached by our starting compositions at values of $F < \sim 0.65$. We also note that the behavior of Ca during melting is secondary to the effects of K when considering evolution of K/Ca as a function of F . Combining equations (S-2) and (S-3) and equations (S-2) and (S-4), and rearranging to solve for C_s/C_o (remembering $D_i = C_i/C_s$), we arrive at two expressions for the composition of residual solid at various degrees of partial melting (Fig. S-5a,b). Taking the ratio of these two expressions, we arrive at our final model for the evolution of $[\text{K}/\text{Ca}]_{\text{solid}}/[\text{K}/\text{Ca}]_o$ during partial melting (Fig. S-5c).

For the most common compositions, the bulk distribution coefficient for K generally decreases as a function of melt fraction (F), and the bulk distribution coefficient for Ca generally increases. However, rocks with high initial $[\text{K}/\text{Ca}]_{\text{protolith}}$ behave in the opposite fashion (Fig. S-5). Although distribution coefficients for K in K-feldspar and for Ca in plagioclase and clinopyroxene are



currently rough approximations, varying them over likely ranges only slightly modifies the results (Fig. S-6), which depend most significantly on $[K/Ca]_{\text{protolith}}$.

Of the seventeen samples plotted in Figure 4 of the main text, two of our granulites fall to the right of our predicted whole rock $[K_2O]_{\text{mdrn}}$ values, which could potentially be a manifestation of incomplete melt segregation. Although it is difficult to calculate the amount of trapped melt required to explain the samples without assuming an arbitrary value for F, the general effect of melt trapping would be to shift data towards the upper right of Figure 4. Additional to melt-trapping, complexities may also arise from variations in the values for $K_d(\text{plag})$ and $K_d(\text{Kspar})$ during melting. Given the same protolith, the distribution coefficients for K and Ca also depend on temperature, pressure, and external fluids, and may change along the course of melting, with lower temperatures favoring higher $[K/Ca]_{\text{melt}}$ (Gao *et al.*, 2016).

Although we cannot directly address the PT conditions of melting with our data, if a non-negligible amount of calcium is lost, our ε_{Ca} measurements suggest that melt-segregation probably occurred during/after the formation of garnet, otherwise large ε_{Ca} signatures would not be fully preserved. This would especially be the case for pelitic samples with low initial $[\text{CaO}]$ — where Ca acts incompatibly during initial melting (see Fig. S-5b). On the other hand, if only minor amounts of Ca are lost, this would preclude any statements addressing the timing of melt-loss, which can occur both before and after peak metamorphic pressure and temperature conditions (Yakymchuk and Brown, 2014). In spite of this uncertainty, our results are in general agreement with melt estimates from other studies, and ~90% of our samples appear to be consistent with our model predictions. Fractional melting models and hybrid-models where melt is removed from the system in batches of ~7% lead to higher melt-fraction estimates for our samples. In order to remain conservative in our minimum melt-loss estimates, and given the uncertainty in melt-loss dynamics, we chose to model our results with a non-modal batch-melting model. Many additional processes, however, have been shown to affect the composition of crustal melts, including entrainment of peritectic/residual minerals (García-Arias, 2018; García-Arias and Stevens, 2017; Sawyer, 2014), diffusion of H_2O and K_2O (Nicoli *et al.*, 2017), and disequilibrium melting (Madlikana and Stevens, 2018).



Supplementary Tables

Table S-1 Modal mineralogy estimates of analysed samples (from optical, X-ray map, and BSE image analyses).

	2030B	2032A	2032I	2033A	2035A	2035B	2036A	2036C	2036E	2038	2040C
Plag	2	-	20	63	-	18	-	6	25	9	-
Cpx	9	-	11	14	8	1	-	-	-	-	-
Opx	89	1	68	23	58	80	-	-	-	-	60
Grt	-	22	-	-	-	-	21	25	36	4	30
Sil	-	6	-	-	-	-	7	11	1	1	-
Qtz	-	?	-	-	-	-	36	33	20	47	10
Crd	-	46	-	-	-	-	20	-	7	-	-
Spr	-	19	-	-	-	-	-	-	-	-	-
Ol	-	-	-	-	16	-	-	-	-	-	-
Hbl	-	-	-	-	14	-	-	-	-	-	-
Bt	1	-	-	-	3	1	-	-	4	-	-
Kspar*	-	6	-	-	-	-	14	25	7	39	-
Ap	-	-	0.6	-	-	-	0.2	-	-	-	-
Spl	-	-	-	-	-	-	1	-	-	-	-
Opqs	0.4	0.1	0.1	0.1	0.5	0.4	0.4	0.5	0.5	0.0	0.2
Rt	-	-	-	-	-	-	-	-	-	-	-
	2044	DDM-163	DDM-303	DDM-309	DDM-342	IV-16-09	IV-16-19	IV-16-24	IZ408-L	IZ408-M	14DLB-39
Plag	16	26	65	52	81	45	20	-	21	41	-
Cpx	-	41	-	22	10	-	-	-	-	-	49
Opx	1	2	1	16	-	-	-	-	-	-	-
Grt	-	31	21	6	8	5	33	30	-	-	34
Sil	-	-	-	-	-	-	-	1	-	-	-
Qtz	42	-	-	-	-	37	-	7	75	-	13
Crd	-	-	-	-	-	-	-	4	-	-	-
Spr	-	-	-	-	-	-	-	-	-	-	-
Ol	-	-	-	-	-	-	-	-	-	-	-
Hbl	1	-	-	2	-	-	47	-	3	53	-
Bt	-	-	2	-	-	11	-	-	-	-	-
Kspar*	40	-	10	-	-	-	-	58	-	-	-
Ap	-	-	-	-	-	-	-	-	-	-	2
Spl	-	-	-	-	-	-	-	-	-	-	-
Opqs	0.0	0.2	1.0	1.8	0.2	1.0	0.8	0.9	0.1	6.1	-
Rt	-	-	-	-	-	-	-	-	-	-	1.7

*K-spar is dominantly perthitic



Table S-2 Whole-rock chemistry (by XRF or EPMA reconstruction*).

	2030B	2032A	2032I	2033A	2035A	2035B	2036A	2036C
SiO ₂	48.5	65.0	58.2	46.6	45.1	58.6	67.0	60.7
TiO ₂	0.3	0.9	0.5	0.1	0.8	0.6	0.8	0.9
Al ₂ O ₃	5.9	19.3	8.0	20.5	4.6	8.3	17.3	19.8
FeO	19.6	6.1	10.4	10.0	18.2	11.1	5.9	8.3
MgO	20.3	6.4	14.5	5.9	22.8	15.2	5.1	3.6
CaO	2.6	0.2	6.6	13.6	4.8	2.3	0.4	0.6
Na ₂ O	0.4	0.6	0.2	1.5	0.4	1.9	0.8	1.6
K ₂ O	0.05	0.81	0.10	0.25	0.90	0.61	1.86	3.58
MnO	0.3	0.1	0.2	0.2	0.3	0.2	0.1	0.1
Mg [#]	64.9	65.3	71.3	51.3	69.1	71.0	60.7	43.4
A/CNK	1.08	8.93	0.63	0.75	0.44	1.05	4.33	2.60
K/Ca	0.02	5.54	0.02	0.02	0.22	0.32	5.69	6.93
	2036E	2038	2040C	2044	DDM163*	DDM303*	DDM309	DDM309*
SiO ₂	51.1	76.2	48.2	74.3	48.9	53.7	47.1	49.4
TiO ₂	0.8	0.1	0.5	0.2	0.4	0.0	1.3	1.3
Al ₂ O ₃	15.2	13.8	8.6	13.6	15.5	24.3	13.7	15.8
FeO	15.9	0.7	19.7	2.1	11.8	6.9	13.0	11.2
MgO	11.1	0.2	20.1	0.4	8.5	3.9	12.8	6.7
CaO	2.1	1.0	0.3	1.6	12.3	3.7	10.1	12.6
Na ₂ O	1.0	2.3	0.0	2.8	2.2	5.8	1.3	2.7
K ₂ O	1.00	5.79	0.004	4.87	0.07	1.69	0.27	0.21
MnO	0.2	0.0	0.2	0.0	0.2	0.1	0.2	0.2
Mg [#]	55.4	29.7	64.5	22.6	56.3	50.3	63.7	51.6
A/CNK	2.33	1.18	13.81	1.06	0.59	1.34	0.66	0.57
K/Ca	0.55	7.08	0.003	3.56	0.01	0.53	0.03	0.02
	DDM342*	IV-16-09	IV-16-19	IV-16-24	IZ408-L	IZ408-M	14DLB39	
SiO ₂	48.5	66.4	42.5	51.4	90.8	45.0	44.1	
TiO ₂	0.4	0.9	1.8	1.7	0.1	3.2	2.1	
Al ₂ O ₃	28.1	16.5	20.7	24.9	5.4	14.6	16.2	
FeO	3.3	5.3	13.5	13.5	0.4	17.2	14.3	
MgO	2.4	1.8	6.7	4.3	0.1	7.1	8.1	
CaO	14.8	7.2	12.1	0.8	1.8	8.7	13.0	
Na ₂ O	2.4	0.4	1.6	1.2	1.3	2.7	1.3	
K ₂ O	0.13	1.33	0.75	2.00	0.13	0.75	0.06	
MnO	0.0	0.1	0.2	0.2	0.0	0.3	0.2	
Mg [#]	57.1	37.5	47.2	36.0	34.2	42.3	50.2	
A/CNK	0.91	1.08	0.81	4.45	0.99	0.69	0.63	
K/Ca	0.01	0.21	0.07	2.89	0.08	0.10	0.005	



Table S-3 Mineral Compositions analysed by EPMA (in wt. %).

	2030B	2032A	2032I	2033A	2035A	2035B	2036A	2036C	2036E	2038	2040C
Garnet											
SiO ₂		40.6					40.6	39.6	40.8	38.4	40.3
TiO ₂		0.03					0.06	0.04	0.06	0.05	0.02
Al ₂ O ₃		23.1					22.6	22.7	23.1	22.0	22.3
FeO		22.9					23.3	24.0	21.7	30.5	23.6
MgO		13.6					13.6	13.0	13.5	7.3	12.9
CaO		0.2					0.7	0.8	1.2	1.1	1.2
Na ₂ O		-					< D.L.	0.01	0.005	-	0.003
K ₂ O		-					0.003	0.001	0.004	-	-
MnO		0.2					0.5	0.2	0.3	0.9	0.5
Cr ₂ O ₃		-					-	-	-	0.004	-
Y ₂ O ₃		-					-	-	-	-	-
Total		100.7					101.3	100.4	100.7	100.1	100.8
Alm %		48.1					47.1	48.1	45.5	66.7	48.0
Pyr %		51.0					49.8	49.1	50.6	28.4	47.9
Grs %		0.4					2.0	2.2	3.1	3.0	3.1
Spsr %		0.5					1.1	0.5	0.7	2.0	1.1
Plagioclase											
SiO ₂	45.0		45.9	47.6		57.8		64.2	58.7	62.1	
TiO ₂	-		0.01	-		0.02		0.01	0.03	-	
Al ₂ O ₃	35.1		35.5	33.7		26.6		21.6	26.7	24.3	
Fe ₂ O ₃	0.15		0.09	0.13		0.15		0.04	0.05	0.02	
CaO	18.1		18.1	16.4		8.0		3.1	8.1	4.8	
Na ₂ O	1.3		1.1	2.1		6.7		7.9	6.3	8.6	
K ₂ O	0.05		0.02	0.20		0.26		2.22	0.31	0.26	
Total	99.6		100.8	100.0		99.4		99.0	100.2	100.1	
An %	88.4		89.8	80.0		39.2		15.4	40.7	23.3	
Ab %	11.3		10.1	18.8		59.2		71.3	57.5	75.2	
Orth %	0.3		0.1	1.2		1.5		13.3	1.8	1.5	
K-feldspar											
SiO ₂							63.7	64.2		64.1	
TiO ₂							-	0.04		-	
Al ₂ O ₃							19.0	19.1		19.1	
Fe ₂ O ₃							0.03	0.01		0.01	
CaO							0.26	0.31		0.05	
Na ₂ O							2.0	2.4		1.0	
K ₂ O							13.9	13.1		15.4	
Total							98.9	99.1		99.7	
An %							1.2	1.6		0.3	
Ab %							17.7	21.3		9.1	
Orth %							81.1	77.1		90.7	



Table S-3 (continued)

	2044	DDM163	DDM303	DDM309	DDM342	IV-16-09	IV-16-19	IV-16-24	IZ408-L	IZ408-M	14DLB39
Garnet											
SiO ₂	39.6	40.3	38.7	39.8	38.0	39.1	39.3				39.8
TiO ₂	0.13	0.02	0.16	0.13	0.02	0.10	0.02				0.08
Al ₂ O ₃	22.0	22.7	21.8	22.2	21.4	21.2	21.7				21.7
FeO	23.6	22.5	26.9	21.3	29.9	24.3	28.6				21.7
MgO	8.8	12.3	6.0	8.9	3.2	7.7	9.3				6.9
CaO	6.3	2.7	6.7	8.2	6.7	6.5	0.8				9.9
Na ₂ O	0.02	0.04	0.02	0.02	-	-	-				-
K ₂ O	< D.L.	< D.L.	0.01	< D.L.	-	-	0.004				0.01
MnO	0.5	0.3	0.8	0.4	1.0	1.0	0.4				0.4
Cr ₂ O ₃	-	-	-	-	0.01	0.01	0.04				0.002
Y ₂ O ₃	-	-	-	-	-	0.01	0.01				0.02
Total	101.0	100.8	101.2	101.0	100.2	99.8	100.2				100.5
Alm %	49.0	46.8	56.7	44.0	66.1	51.2	61.5				46.0
Pyr %	32.9	45.5	23.1	33.1	12.7	29.1	35.5				26.2
Grs %	17.1	7.2	18.5	22.1	18.9	17.4	2.3				26.9
Spsr %	1.1	0.6	1.8	0.8	2.3	2.1	0.8				0.9
Plagioclase											
SiO ₂	61.4	60.3	63.0	55.3	50.1	45.2	48.8		66.2	56.2	
TiO ₂	-	-	-	0.01	-	-	-		-	-	
Al ₂ O ₃	24.4	26.0	23.8	28.1	32.8	35.8	33.0		21.4	28.2	
Fe ₂ O ₃	0.17	0.03	0.03	0.07	0.06	0.03	0.38		0.17	0.09	
CaO	5.2	7.1	4.5	10.1	14.7	18.2	14.6		1.4	9.2	
Na ₂ O	8.0	7.5	8.9	5.5	3.0	1.1	2.9		10.6	6.1	
K ₂ O	0.77	0.33	0.35	0.34	0.17	0.01	0.16		0.25	0.09	
Total	99.9	101.1	100.6	99.5	100.8	100.4	99.8		100.0	100.0	
An %	25.3	33.5	21.4	49.3	72.5	90.0	72.8		6.5	45.1	
Ab %	70.2	64.6	76.6	48.7	26.5	10.0	26.3		92.1	54.3	
Orth %	4.5	1.9	2.0	2.0	1.0	0.1	0.9		1.4	0.5	
K-feldspar											
SiO ₂	63.8							61.9			
TiO ₂	-							-			
Al ₂ O ₃	19.0							18.9			
Fe ₂ O ₃	0.03							0.10			
CaO	0.11							0.16			
Na ₂ O	1.3							1.9			
K ₂ O	14.7							14.1			
Total	99.1							97.0			
An %	0.6							0.8			
Ab %	12.1							16.7			
Orth %	87.3							82.5			



Table S-4 Mineral-separate compositions (by ICP-OES, double-spike[†], and mixed-spike TIMS[‡]).

	2032A	2032I	2035A	2035B	2036A	2036C	2038
Garnet Separates							
Ca (wt. %)	0.09				0.49	0.51	0.70
K (wt. %)	0.02				0.05	0.003	0.02
MgO (wt. %)*	9.9				13.5	11.7	7.3
Na ₂ O (wt. %)*	0.01				0.003	<D.L.	0.004
K/Ca (mol/mol)	0.18				0.09	0.01	0.03
Ca (wt. %) [†]	0.11				0.54	0.58	0.70
⁴⁴ Ca (mol) [†]	5.5E-05				2.8E-04	3.0E-04	3.6E-04
Ca (wt. %) [‡]	-				-	-	0.65
K (wt. %) [‡]	-				-	-	0.03
Feldspar Separates							
Ca (wt. %)		11.41		3.49		0.49	0.89
K (wt. %)		0.27		0.55		8.21	8.65
MgO (wt. %)*		1.3		1.5		<D.L.	0.02
Na ₂ O (wt. %)*		1.0		4.7		3.2	3.6
K/Ca (mol/mol)		0.02		0.16		17.1	10.0
Ca (wt. %) [†]		12.72		3.99		0.68	0.88
⁴⁴ Ca (mol) [†]		6.5E-03		2.1E-03		3.5E-04	4.5E-04
Ca (wt. %) [‡]		-		-		-	0.76
K (wt. %) [‡]		-		-		-	6.67
Whole Rocks							
Ca (wt. %)	-	4.99	3.12	1.32	0.16	0.30	0.73
K (wt. %)	-	0.08	0.77	0.46	1.39	2.48	5.38
MgO (wt. %)*	-	15.4	17.3	13.4	4.6	3.5	0.2
Na ₂ O (wt. %)*	-	0.2	0.5	1.9	0.3	1.0	2.6
K/Ca (mol/mol)	-	0.02	0.25	0.4	8.8	8.4	7.6
Ca (wt. %) [†]	0.035	4.71	3.48	1.54	0.18	0.33	0.69
⁴⁴ Ca (mol) [†]	1.8E-05	2.4E-03	1.8E-03	8.0E-04	9.0E-05	1.7E-04	3.5E-04
Ca (wt. %) [‡]	0.035	-	-	-	0.063	-	0.56
K (wt. %) [‡]	0.539	-	-	-	0.49	-	3.62

[†]measurement using ⁴²Ca-⁴⁸Ca double spike (TIMS); [‡]measurement using ⁴¹K-⁴³Ca mixed-spike (ID-TIMS),

*value converted to oxide (wt. %) for easier comparison to other analyses.



Table S-4 (continued)

	2044	DDM303	IV-16-09	IV-16-24	IZ408-L	IZ408-M	14DLB39
Garnet Separates							
Ca (wt. %)		1.73		0.47			7.72
K (wt. %)		<D.L.		0.08			0.01
MgO (wt. %)*		13.9		8.2			7.4
Na ₂ O (wt; %)*		0.03		0.03			0.17
K/Ca (mol/mol)		-		0.15			0.001
Ca (wt. %)†		1.70		0.54			7.22
⁴⁴ Ca (mol)†		8.7E-04		2.8E-04			3.7E-03
Ca (wt. %)‡		-		0.37			-
K (wt; %)‡		-		0.05			-
Feldspar Separates							
Ca (wt. %)		2.66		0.56			
K (wt. %)		0.65		3.76			
MgO (wt. %)*		1.5		0.1			
Na ₂ O (wt. %)*		6.8		3.3			
K/Ca (mol/mol)		0.25		6.8			
Ca (wt. %)†		3.01		0.63			
⁴⁴ Ca (mol)†		1.5E-03		3.2E-04			
Whole Rocks							
Ca (wt. %)	1.17		5.78	0.62	1.33	6.94	9.72
K (wt. %)	4.11		1.26	1.68	0.10	0.62	0.03
MgO (wt. %)*	0.3		2.2	5.0	0.1	8.4	9.1
Na ₂ O (wt. %)*	3.0		0.4	1.2	1.3	2.7	1.4
K/Ca (mol/mol)	3.6		0.22	2.8	0.08	0.09	0.003
Ca (wt. %)†	1.17		5.42	0.60	1.29	6.36	-
⁴⁴ Ca (mol)†	6.0E-04		2.8E-03	3.1E-04	6.6E-04	3.3E-03	-
Ca (wt. %)‡	1.22		-	0.53	-	-	-
K (wt. %)‡	4.10		-	1.32	-	-	-

†measurement using ⁴²Ca-⁴⁸Ca double spike (TIMS); ‡measurement using ⁴¹K-⁴³Ca mixed-spike (ID-TIMS),

*value converted to oxide (wt. %) for easier comparison to other analyses.



Table S-5 ϵ_{Ca} of analysed standards (analysed by TIMS).

Sample	Type	Notes	$^{40}\text{Ca}/^{44}\text{Ca}$	SE (Abs)	ϵ_{Ca}		Sample	Type	Notes	$^{40}\text{Ca}/^{44}\text{Ca}$	SE (Abs)	ϵ_{Ca}		
SRM915a	WR	NC	47.161	0.001	1.0		Lost-City	BH2	C	47.163	0.001	1.4		
	WR	NC	47.161	0.006	1.1			BH2	C	47.157	0.001	0.3		
	WR	NC	47.161	0.001	1.0			BH2	C	47.155	0.001	-0.2		
	WR	C	47.164	0.001	1.6			BH2	C	47.150	0.001	-1.3		
	WR	NC	47.165	0.001	1.9			BH2	C	47.153	0.001	-0.6		
	WR	C	47.157	0.001	0.1			BH2	C	47.157	0.001	0.1		
	WR	C	47.165	0.001	2.0			BH2	NC	47.155	0.001	-0.2		
	WR	NC	47.161	0.001	1.1			Average 2SE	47.156 0.003	-	-0.1	0.6		
	WR	NC	47.165	0.002	1.9									
	WR	C	47.166	0.001	2.2		DNC-1	WR	C	47.150	0.001	-1.3		
	WR	NC	47.162	0.001	1.2			WR	C	47.155	0.001	-0.3		
	WR	C	47.156	0.002	0.1			WR	C	47.152	0.001	-0.9		
	WR	NC	47.168	0.001	2.6			WR	C	47.160	0.001	0.9		
	WR	C	47.168	0.001	2.6			WR	C	47.157	0.001	0.1		
	WR	NC	47.159	0.001	0.7			WR	C	47.159	0.001	0.6		
	WR	NC	47.162	0.001	1.2			WR	C	47.159	0.001	0.5		
	WR	NC	47.166	0.001	2.1			WR	C	47.158	0.001	0.3		
	WR	NC	47.166	0.001	2.1			WR	C	47.160	0.001	0.8		
	Average 2SE	47.163 0.002	-	1.5 0.4		WR	WR	WR	WR	WR	WR	WR	WR	
W2A	WR	C	47.152	0.001	-0.8			(n = 24)	Average 2SE	47.156 0.001	-	0.0	0.3	
	WR	C	47.154	0.001	-0.3									
	WR	C	47.157	0.002	0.2									
	WR	C	47.156	0.001	0.0									
	WR	C	47.149	0.001	-1.4									
	WR	C	47.162	0.001	1.2									
	WR	C	47.155	0.001	-0.1									
	WR	C	47.157	0.002	0.1									
	Average 2SE	47.155 0.003	-	-0.1 0.5										

*Bulk Silicate Earth (BSE) defined by Lost City vent fluids (BH2) and dolerite standards DNC-1 & W2A.

C - Column chemistry performed; NC - no column chemistry performed



Table S-5 (continued)

Sample	Type	Aliquot	$^{40}\text{Ca}/^{44}\text{Ca}$	SE (Abs)	ε_{Ca}		Sample	Type	Aliquot	$^{40}\text{Ca}/^{44}\text{Ca}$	SE (Abs)	ε_{Ca}	
2030B	plag	A	47.173	0.001	3.6	3.1	2040C	WR	A	47.215	0.001	12.5	12.5
	plag	B	47.168	0.001	2.6			WR	B	47.215	0.001	12.5	
2032A	WR	A	47.514	0.002	76.0	76.8	2044	grt	A	47.213	0.001	12.1	12.5
	WR	B	47.515	0.002	76.1			grt	B	47.217	0.001	12.9	
	WR	C	47.520	0.002	77.3			WR	A	47.225	0.001	14.5	14.9
	WR	D	47.518	0.003	76.7		DDM163	WR	B	47.228	0.001	15.3	
	WR-2	A	47.523	0.001	77.8			grt	A	47.161	0.001	1.1	
	grt	A	47.356	0.001	42.4			grt	B	47.155	0.001	-0.2	
	grt	B	47.356	0.001	42.4			grt	C	47.158	0.002	0.3	0.4
2032I	plag	A	47.165	0.001	1.9	2.0	DDM303	grt	A	47.167	0.001	2.4	2.4
	plag	B	47.166	0.001	2.1			grt	B	47.167	0.002	2.3	
2033A	plag	A	47.172	0.001	3.4	2.3	DDM309	grt	A	47.153	0.001	-0.6	
	plag	B	47.161	0.002	1.2			grt	B	47.157	0.001	0.3	
2035A	WR	A	47.163	0.001	1.5	2.4	DDM342	grt	C	47.153	0.001	-0.6	-0.3
	WR	B	47.172	0.001	3.4			grt	A	47.163	0.003	1.5	
2035B	WR	A	47.175	0.001	3.9	3.5	IV-16-09	grt	B	47.165	0.001	2.0	1.8
	WR	B	47.171	0.001	3.1			grt	A	47.157	0.001	0.3	
	plag	A	47.169	0.001	2.9			WR	B	47.163	0.001	1.5	
	plag	B	47.174	0.001	3.8			grt	A	47.164	0.002	1.6	
2036A	WR	A	47.344	0.001	39.8	39.6	IV-16-19	grt	B	47.163	0.001	1.4	1.5
	WR	B	47.341	0.001	39.3			grt	B	47.163	0.001	1.4	
	grt	A	47.217	0.001	13.0			WR	A	47.162	0.001	1.2	
	grt	B	47.231	0.001	16.0			WR	B	47.160	0.001	0.8	1.0
	grt	C	47.231	0.001	15.9			grt	A	47.160	0.002	0.9	
	grt	D	47.233	0.001	16.3			grt	B	47.159	0.002	0.6	0.7
2036C	WR	A	47.329	0.001	36.8	36.3	IV-16-24	WR	A	47.172	0.001	3.4	2.9
	WR	B	47.321	0.001	35.1			WR	B	47.167	0.001	2.4	
	WR	C	47.331	0.001	37.1			grt	A	47.170	0.001	2.9	
	Kspar	A	47.427	0.001	57.4			grt	B	47.164	0.001	1.7	2.3
	Kspar	B	47.432	0.001	58.5			Kspar	A	47.173	0.003	3.5	
	grt	A	47.215	0.001	12.4			Kspar	B	47.171	0.001	3.1	
	grt	B	47.216	0.001	12.8			Kspar	C	47.181	0.003	5.3	4.2
2036E	WR	A	47.184	0.001	5.8	6.9	IZ408-L	WR	A	47.161	0.001	1.0	1.4
	WR	B	47.187	0.001	6.6			WR	B	47.164	0.001	1.8	
	WR	C	47.196	0.001	8.4		IZ408-M	WR	A	47.164	0.002	1.7	1.0
	grt	A	47.177	0.001	4.4			WR	B	47.157	0.001	0.3	
	grt	B	47.176	0.001	4.2								
2038	WR	A	47.312	0.001	33.1	34.1	14DLB39	grt	A	47.162	0.001	1.3	1.1
	WR	B	47.321	0.001	35.0			grt	B	47.160	0.002	0.9	
	WR	C	47.318	0.001	34.3		Kspar	A	47.345	0.001	40.2		
	Kspar	A	47.345	0.001	40.2			B	47.350	0.001	41.2		
	Kspar	B	47.350	0.001	41.2			A	47.222	0.001	14.0		
	grt	A	47.222	0.001	14.0			B	47.225	0.001	14.7		
	grt	B	47.220	0.001	13.7			C	47.220	0.001	14.1		

note: ε_{Ca} values are normalised to BSE ($^{40}\text{Ca}/^{44}\text{Ca} = 47.156$)

Table S-6 Selected results from anhydrous melting experiments at ~900 C and ~1.0 GPa with various starting materials, taken from (Gao *et al.*, 2016) references (Castro *et al.*, 1999, 2000; Patiño Douce and Beard, 1995; Pickering and Johnston, 1998; Rapp *et al.*, 1991; Skjerlie *et al.*, 1993; Skjerlie and Johnston, 1992, 1993, 1996; Watkins *et al.*, 2007).

	pelite	two-mica metapelite	two-mica gneiss	Bt gneiss	tonalite	tonalite	tonalite	Bt tonalite	Hbl tonalite	Hbl tonalite	Metavolcanoclastic	ophiolite	qtz amphibolite
T (°C)	900	900	900	900	900	900	875	875	875	875	900	900	900
P (kbar)	10	10	10	10	10	10	10	10	10	11	10	8	10
<i>Starting Compositions</i>													
SiO ₂	57.36	77.14	69.10	67.02	68.30	67.05	68.26	70.12	68.98	68.98	59.03	51.19	60.40
TiO ₂	1.26	0.50	0.52	0.41	0.50	0.48	0.52	0.29	0.35	0.35	1.12	1.18	1.70
Al ₂ O ₃	23.24	11.20	15.20	16.98	14.90	15.19	14.89	16.18	16.07	16.07	15.12	16.62	11.30
FeO (T)	8.59	3.39	3.77	-	4.70	3.84	4.67	2.07	2.54	2.54	13.00	11.32	7.90
MnO	0.17	-	0.04	0.04	0.10	0.04	0.06	0.02	0.03	0.03	0.16	0.23	0.20
MgO	2.72	1.23	1.51	0.60	1.70	1.88	1.73	0.77	1.00	1.00	2.48	6.59	6.70
CaO	0.40	0.75	1.28	3.18	2.90	2.56	2.93	2.69	3.77	3.77	5.31	5.49	7.60
Na ₂ O	0.48	1.42	3.06	4.09	4.50	4.83	4.47	5.31	5.29	5.29	3.28	4.33	1.90
K ₂ O	3.63	2.44	3.81	3.62	2.10	1.85	2.05	1.81	1.53	1.53	1.64	0.82	0.70
P ₂ O ₅	-	-	-	0.20	0.20	0.13	0.15	-	-	-	0.20	-	-
K/Ca	10.54	3.78	3.46	1.32	0.84	0.84	0.81	0.78	0.47	0.47	0.36	0.17	0.11
A/CNK	4.27	1.77	1.32	1.03	1.00	1.04	1.00	1.04	0.93	0.93	0.90	0.92	0.64
Mg#	36.08	39.27	41.66	-	39.20	46.60	39.77	39.87	41.24	41.24	25.38	50.93	60.19
<i>Melt Compositions</i>													
SiO ₂	75.35	74.13	74.11	73.59	73.48	73.42	74.27	76.00	76.29	75.62	74.65	64.52	76.22
TiO ₂	0.22	0.20	0.17	0.33	0.10	0.07	0.07	0.10	0.19	0.16	0.22	0.47	0.34
Al ₂ O ₃	14.18	15.55	15.90	14.80	14.88	14.89	15.26	13.92	13.45	13.47	15.17	19.62	14.92
FeO (T)	1.70	1.39	1.41	1.26	1.26	1.24	1.25	1.58	1.59	1.51	2.03	4.45	2.01
MnO	0.03	<D.L.	0.07	0.03	<D.L.	0.04	0.03	0.04	0.08	0.15	0.02	<D.L.	0.06
MgO	0.43	0.28	0.22	0.13	0.10	0.13	0.13	0.18	0.17	0.35	0.20	1.24	0.50
CaO	0.24	0.83	0.70	0.93	1.05	1.03	1.16	1.43	1.19	1.42	1.66	3.15	2.81
Na ₂ O	1.36	2.13	3.49	4.20	4.61	4.67	3.89	3.32	2.91	3.23	1.92	5.35	0.95
K ₂ O	6.38	5.23	3.93	4.73	4.51	4.49	3.89	3.44	4.13	4.11	4.05	1.20	2.17
P ₂ O ₅	0.11	0.24	-	-	-	0.03	0.03	-	-	-	0.07	-	-
K/Ca	30.60	7.29	6.52	5.91	4.99	5.08	3.89	2.78	4.03	3.37	2.83	0.44	0.90
A/CNK	1.48	1.46	1.41	1.08	1.04	1.03	1.20	1.18	1.18	1.09	1.44	1.24	1.65
Mg#	31.22	26.72	21.76	15.53	12.93	15.34	15.34	16.56	15.68	29.07	14.94	33.24	30.72



Supplementary Figures

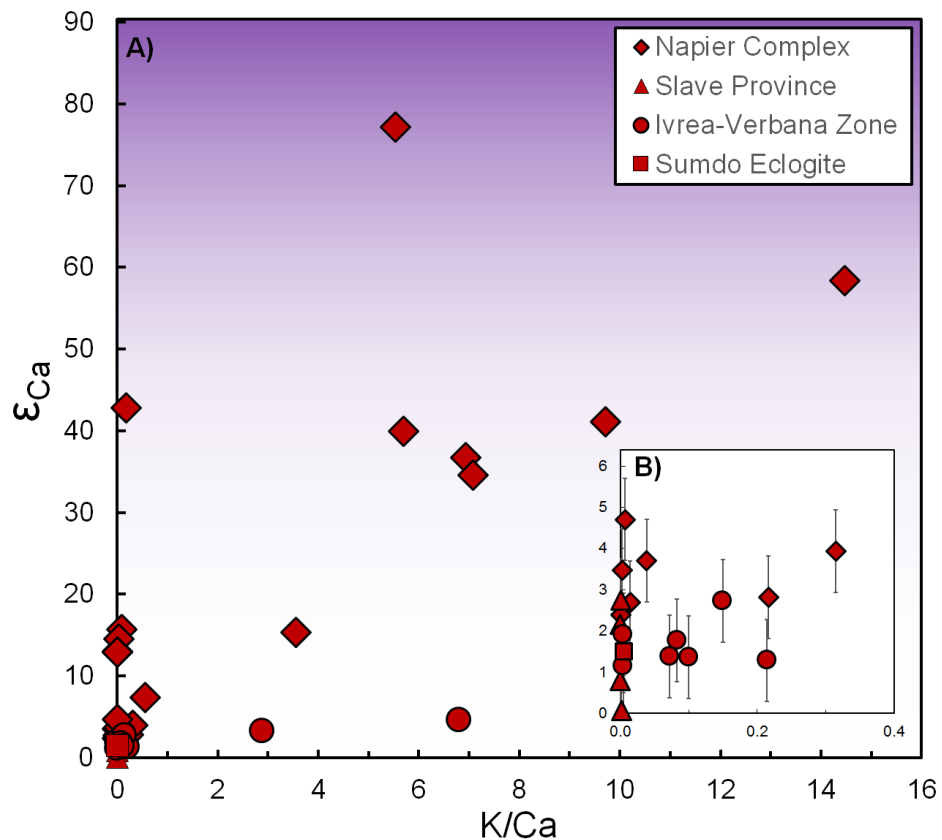


Figure S-1 ϵ_{Ca} vs. modern K/Ca (measured by XRF, ICP-OES, or ID-TIMS) for all measured samples in this study ($n = 35$), differentiated by location as indicated in the legend. Inset (b) has the same axes as A, but is zoomed in to show the finer variability between samples. Horizontal error bars are smaller than the symbols, vertical error bars are ± 1 (see methods for discussion).



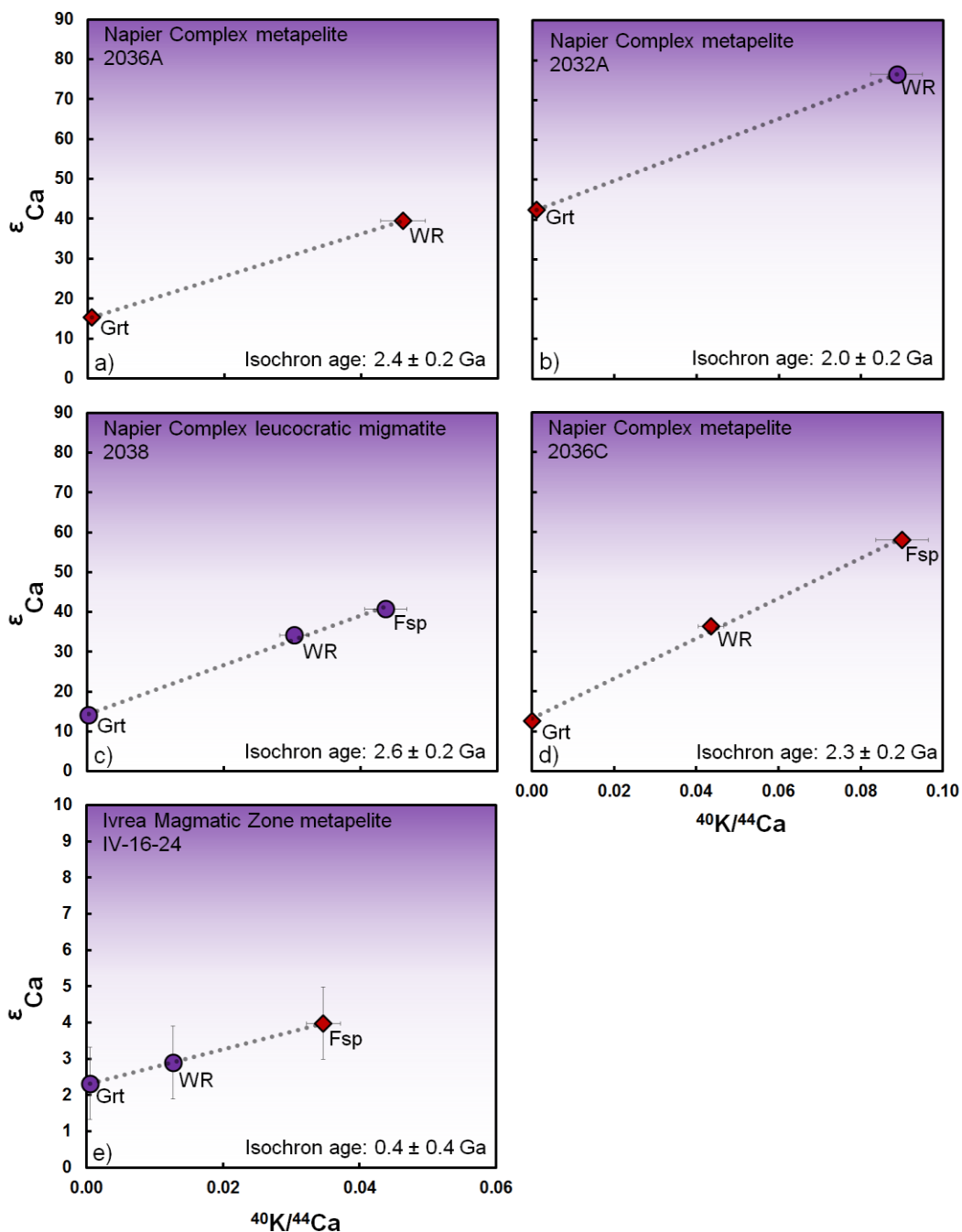


Figure S-2 ^{40}K - ^{40}Ca isochrons for samples from the Napier Complex, Antarctica, and from the Ivrea-Verbano Zone, Italy. Potassium concentrations measured by ICP-OES (purple diamonds) or ID-TIMS (red diamonds), [^{44}Ca] concentrations calculated from double-spike TIMS analyses (Table S-4).



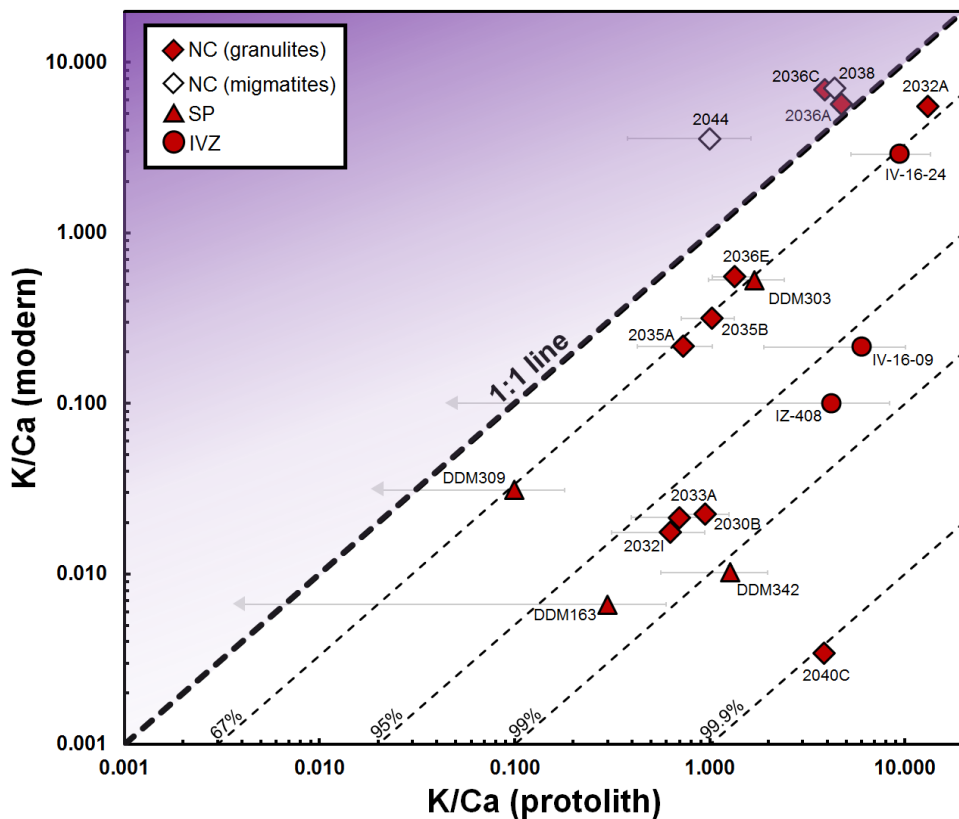


Figure S-3 Whole rock K/Ca measured in modern samples versus ϵ_{Ca} -based K/Ca estimates in protolith rocks [from equation (2)]. NC granulite samples ($n = 10$), NC migmatites ($n = 2$), SP samples ($n = 4$), IVZ samples ($n = 3$). Contours indicate relative K-loss (in %) assuming constant Ca. Uncertainties in protolith K/Ca are calculated using equation (2), taking into account ages for each sample and our 2SD on ϵ_{Ca} (± 1); arrow terminations represent samples within error of BSE. Uncertainties for modern K/Ca (measured by XRF, $< \sim 5\%$) are smaller than the symbols.



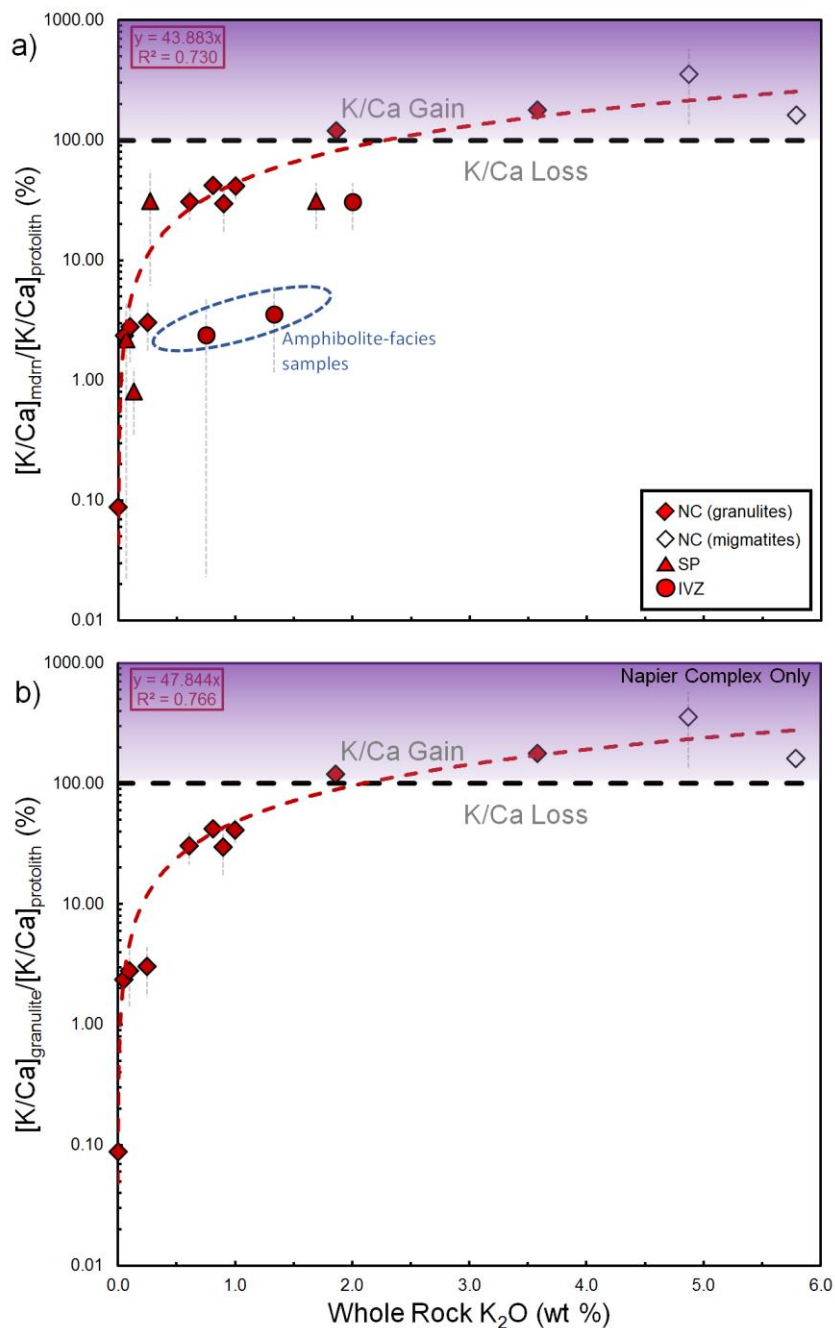


Figure S-4 Linear regressions of $[K/Ca]_{\text{mdrn}}/[K/Ca]_{\text{protolith}}$ vs. whole rock K_2O (wt. %) for (a) all samples (excluding IV-16-19 and 14DLB39) and for (b) Napier Complex samples only. Symbols and uncertainties are the same as in Figure 4 of the main text. NC granulite samples ($n = 10$), NC migmatite samples ($n = 2$), SP samples ($n = 4$), IVZ samples ($n = 3$). Regressions are forced through the origin.)



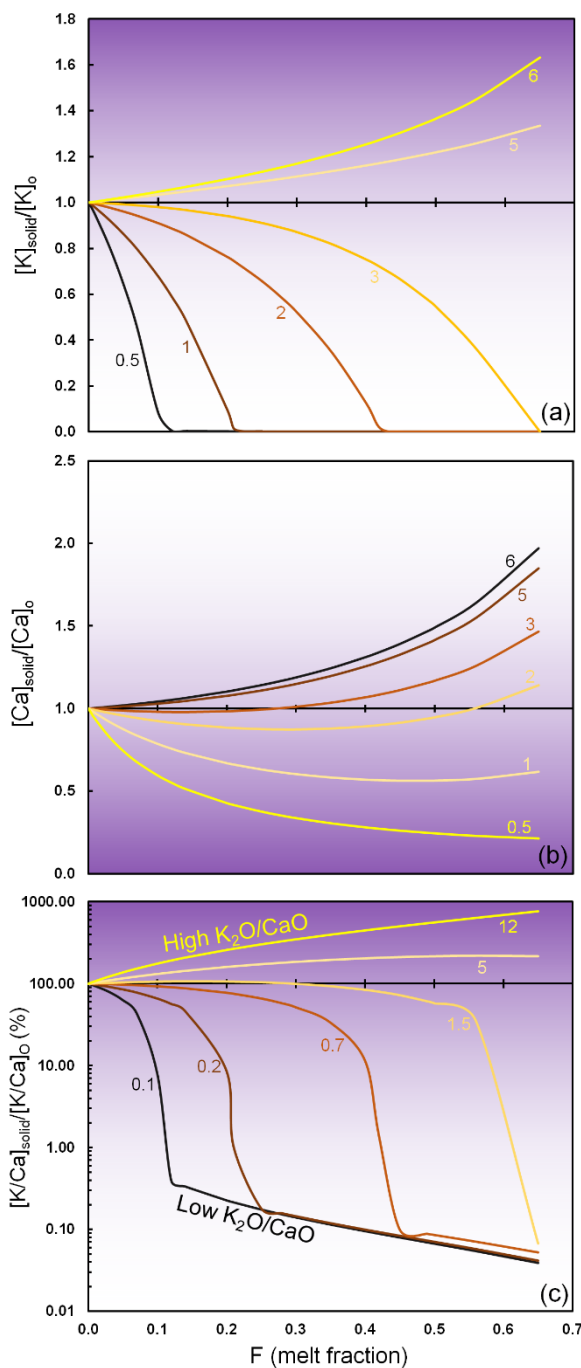


Figure S-5 Model calculations for (a) $[K]_{\text{solid}}/[K]_o$, (b) $[Ca]_{\text{solid}}/[Ca]_o$, and (c) $[K/Ca]_{\text{solid}}/[K/Ca]_o$ for different hypothetical protolith compositions, based on non-modal batch melting model [equations (S-2) through (S-4)]. In a) lines are labeled with starting whole-rock K_2O (wt. %), in b) lines are labelled with starting CaO (wt. %). In c), the lines are labeled with starting K_2O/CaO (wt/wt). Bulk D_K is a function of remaining K-feldspar, and bulk D_{Ca} is a function of remaining plagioclase + clinopyroxene (Methods). K_d/K for K-feldspar = 4 and K_d/Ca for plagioclase & clinopyroxene = 4.



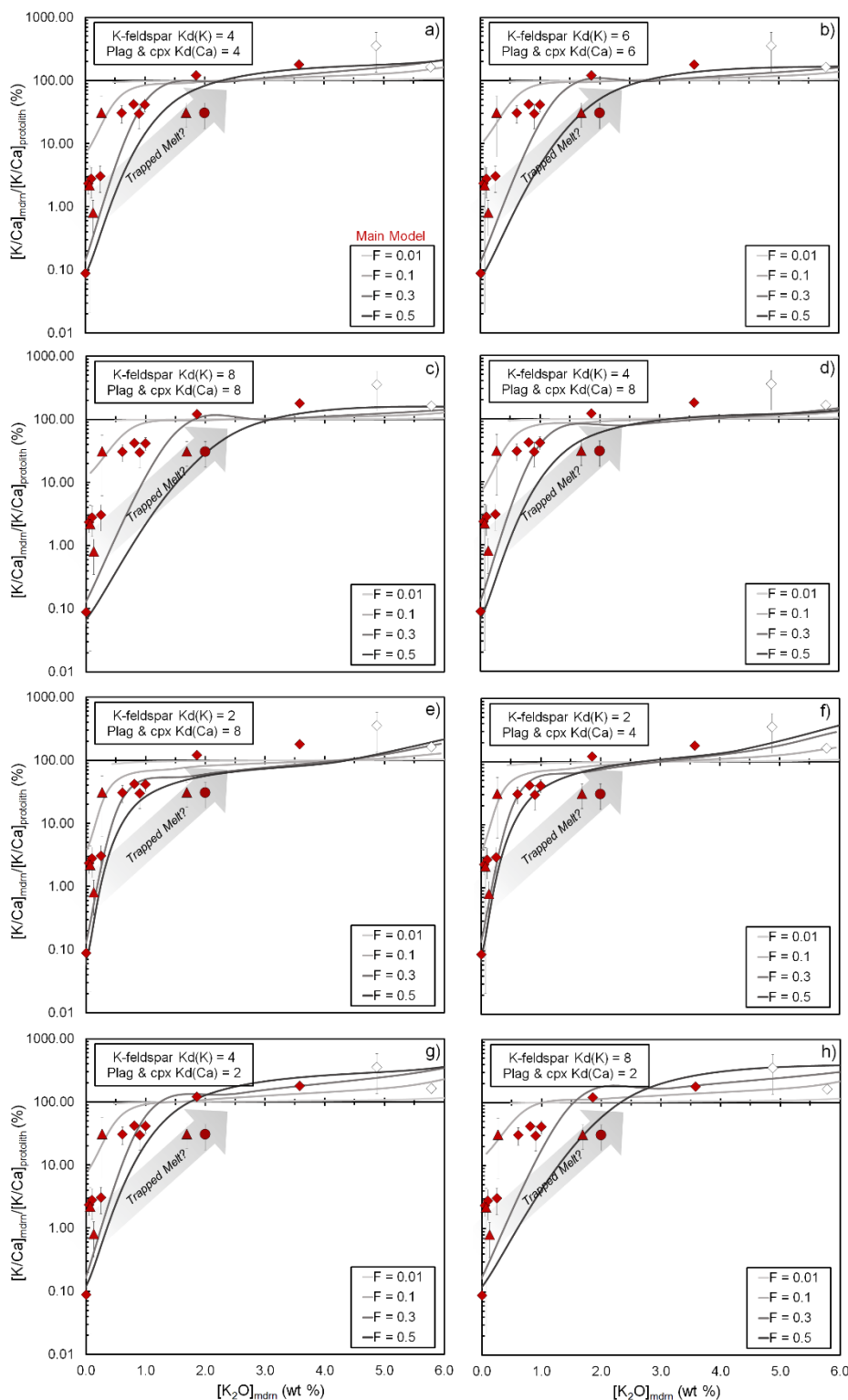


Figure S-6 Melting model results with different distribution coefficients, using equations (3-5) in the main text. In (a-c) we show the effects of increasing both $K_d(K)$ and $K_d(Ca)$ equally. In (d,e) we show the effects of decreasing $K_d(K)$, and in (f-h) the effects of increasing $K_d(K)$ [relative to $K_d(Ca)$].



Supplementary Information References

- Aulbach, S., Krauss, C., Creaser, R.A., Stachel, T., Heaman, L.M., Matveev, S., Chacko, T. (2010) Granulite sulphides as tracers of lower crustal origin and evolution: An example from the Slave craton, Canada. *Geochimica et Cosmochimica Acta* 74, 5368–5381.
- Bartoli, O., Acosta-Vigil, A., Ferrero, S., Cesare, B. (2016) Granitoid magmas preserved as melt inclusions in high-grade metamorphic rocks. *American Mineralogist* 101, 1543–1559.
- Brown, M. (2006) Duality of thermal regimes is the distinctive characteristics of plate tectonics since the Neoarchean. *Geology* 34, 961–964.
- Brown, M. (2007) Metamorphic Conditions in Orogenic Belts: A Record of Secular Change. *International Geology Review* 49, 193–234.
- Castro, A., Corretgé, L.G., El-Biad, M., El-Hmidi, H., Ferrández, C., Patiño Douce, A.E. (2000) Experimental constraints on Hercynian anatexis in the Iberian Massif, Spain. *Journal of Petrology* 41, 1471–1488.
- Castro, A., Patiño Douce, A.E., Corretgé, L.G., De La Rosa, J.D., El-Biad, M., El-Hmidi, H.H. (1999) Origin of peraluminous granites and granodiorites, Iberian massif, Spain: An experimental test of granite petrogenesis. *Contributions to Mineralogy and Petrology* 135, 255–276.
- Davis, W.J., Canil, D., MacKenzie, J.M., Carbone, G.B. (2003) Petrology and U–Pb geochronology of lower crustal xenoliths and the development of a craton, Slave Province, Canada. *Lithos* 71, 541–573.
- DePaolo, D.J., Manton, W.I., Grew, E.S., Halpern, M. (1982) Sm–Nd, Rb–Sr and U–Th–Pb systematics of granulite facies rocks from Fyfe Hills, Enderby Land, Antarctica. *Nature* 298, 614–618.
- Ewing, T.A., Hermann, J., Rubatto, D. (2013) The robustness of the Zr-in-rutile and Ti-in-zircon thermometers during high-temperature metamorphism (Ivrea-Verbano Zone, northern Italy). *Contributions to Mineralogy and Petrology*.
- Farquhar, J., Chacko, T., Ellis, D.J. (1996) Preservation of oxygen isotope compositions in granulites from Northwestern Canada and Enderby Land, Antarctica: implications for high-temperature isotopic thermometry. *Contributions to Mineralogy and Petrology* 125, 213–224.
- Frost, B.R., Chacko, T. (1989) The Granulite Uncertainty Principle: Limitations on Thermobarometry in Granulites. *The Journal of Geology* 97, 435–450.
- Gao, P., Zheng, Y.F., Zhao, Z.F. (2016) Experimental melts from crustal rocks: A lithochemical constraint on granite petrogenesis. *Lithos* 266–267, 133–157.
- Garcia-Arias, M. (2018) Decoupled Ca and Fe + Mg content of S-type granites: An investigation on the factors that control the Ca budget of S-type granites. *Lithos* 318–319, 30–46.
- Garcia-Arias, M., Stevens, G. (2017) Phase equilibrium modelling of granite magma petrogenesis: A. An evaluation of the magma compositions produced by crystal entrainment in the source. *Lithos* 277, 131–153.
- Harley, S.L. (2016) A matter of time: The importance of the duration of UHT metamorphism. *Journal of Mineralogical and Petrological Sciences* 111, 50–72.
- He, Y., Wang, Y., Zhu, C., Huang, S., Li, S. (2016) Mass-Independent and Mass-Dependent Ca Isotopic Compositions of Thirteen Geological Reference Materials Measured by Thermal Ionisation Mass Spectrometry. *Geostandards and Geoanalytical Research* 1–20.
- Hermann, J., Rubatto, D. (2014) *Subduction of Continental Crust to Mantle Depth: Geochemistry of Ultrahigh-Pressure Rocks. Geochemistry of Ultrahigh-Pressure Rocks. Treatise on Geochemistry: Second Edition*. Elsevier Ltd, Oxford.
- Horie, K., Hokada, T., Hiroi, Y., Motoyoshi, Y., Shiraishi, K. (2012) Contrasting Archaean crustal records in western part of the Napier Complex, East Antarctica: New constraints from SHRIMP geochronology. *Gondwana Research*. International Association for Gondwana Research 21, 829–837.
- Kelly, N.M., Harley, S.L. (2005) An integrated microtextural and chemical approach to zircon geochronology: Refining the Archaean history of the Napier Complex, east Antarctica. *Contributions to Mineralogy and Petrology* 149, 57–84.
- Kelsey, D.E., Hand, M. (2015) On ultrahigh temperature crustal metamorphism: Phase equilibria, trace element thermometry, bulk composition, heat sources, timescales and tectonic settings. *Geoscience Frontiers* 6, 311–356.
- Kunz, B.E., Regis, D., Engi, M. (2018) Zircon ages in granulite facies rocks: decoupling from geochemistry above 850 °C? *Contributions to Mineralogy and Petrology* 173, 1–21.
- Kusiak, M.A., Whitehouse, M.J., Wilde, S.A., Dunkley, D.J., Menneken, M., Nemchin, A. a., Clark, C. (2013) Changes in zircon chemistry during Archean UHT metamorphism in the Napier Complex, Antarctica. *American Journal of Science* 313, 933–967.
- Madlakana, N., Stevens, G. (2018) Plagioclase disequilibrium induced during fluid-absent biotite-breakdown melting in metapelites. *Journal of Metamorphic Geology*.
- Marshall, B.D., DePaolo, D.J. (1982) Precise age determinations and petrogenetic studies using the KCa method. *Geochimica et Cosmochimica Acta* 46, 2537–2545.
- Marshall, B.D., DePaolo, D.J. (1989) Calcium isotopes in igneous rocks and the origin of granite. *Geochimica et Cosmochimica Acta* 53, 917–922.
- Mills, R.D., Simon, J.I., DePaolo, D.J. (2018) Calcium and neodymium radiogenic isotopes of igneous rocks: Tracing crustal contributions in felsic magmas related to super-eruptions and continental rifting. *Earth and Planetary Science Letters* 495, 242–250.
- Mitchell, R.J., Harley, S.L. (2017) Zr-in-rutile resetting in aluminosilicate bearing ultra-high temperature granulites: Refining the record of cooling and hydration in the Napier Complex, Antarctica. *Lithos* 272–273, 128–146.
- Nicolai, G., Stevens, G., Moyen, J.F., Vezinet, A., Mayne, M. (2017) Insights into the complexity of crustal differentiation: K2O-poor leucosomes within metasedimentary migmatites from the Southern Marginal Zone of the Limpopo Belt, South Africa. *Journal of Metamorphic Geology* 35, 999–1022.
- Pape, J., Mezger, K., Robyr, M. (2016) A systematic evaluation of the Zr-in-rutile thermometer in ultra-high temperature (UHT) rocks. *Contributions to Mineralogy and Petrology* 171, 1–20.
- Patiño Douce, A.E., Beard, J.S. (1995) Dehydrations-melting of Biotite Gneiss and Quartz Amphibolite from 3 to 15 kbar. *Journal of Petrology* 36, 707–738.
- Pehrsson, S.J., Chacko, T., Pilkington, M., Villeneuve, M.E., Bethune, K. (2000) Anton terrane revisited: Late Archean exhumation of a moderate pressure granulite terrane in the Western Slave Province. *Geology* 28, 1075–1078.
- Pickering, J.M., Johnston, A.D. (1998) Fluid-absent melting behavior of a two-mica metapelite: Experimental constraints on the origin of Black Hills granite. *Journal of Petrology* 39, 1787–1804.
- Pownall, J.M., Hall, R., Armstrong, R.A., Forster, M.A. (2014) Earth's youngest known ultrahigh-temperature granulites discovered on Seram, eastern Indonesia. *Geology* 42, 279–282.
- Rapp, R.P., Watson, E.B., Miller, C.F. (1991) Partial melting of amphibolite/eclogite and the origin of Archean trondhjemites and tonalites. *Precambrian Research* 51, 1–25.
- Redler, C., Johnson, T.E., White, R.W., Kunz, B.E. (2012) Phase equilibrium constraints on a deep crustal metamorphic field gradient: Metapelitic rocks from the Ivrea Zone (NW Italy). *Journal of Metamorphic Geology* 30, 235–254.
- Sawyer, E.W. (2014) The inception and growth of leucosomes: Microstructure at the start of melt segregation in migmatites. *Journal of Metamorphic Geology* 32, 695–712.



- Schiller, M., Paton, C., Bizzarro, M. (2012) Calcium isotope measurement by combined HR-MC-ICPMS and TIMS. *J. Anal. At. Spectrom.* 27, 38–49.
- Simon, J.I., DePaolo, D.J., Moynier, F. (2009) Calcium Isotope Composition of Meteorites, Earth, and Mars. *The Astrophysical Journal* 702, 707–715.
- Skjerlie, K.P., Johnston, A.D. (1992) Vapor-absent melting at 10 kbar of a biotite- and amphibole-bearing tonalitic gneiss—Implications for the generation of A-type granites—Comment and Reply.pdf. *Geology* 20, 263–266.
- Skjerlie, K.P., Johnston, A.D. (1993) Fluid-absent melting behavior of an F-rich tonalitic gneiss at mid-crustal pressures: Implications for the generation of anorogenic granites. *Journal of Petrology* 34, 785–815.
- Skjerlie, K.P., Johnston, A.D. (1996) Vapour absent melting from 10–20 kbar of crustal rock that contain multiple hydrous phase: implications for anatexis in the deep to very deep continental crust and active continental margins. *Journal of Petrology* 37, 661–691.
- Skjerlie, K.P., Patiño Douce, A.E., Johnston, A.D. (1993) Fluid absent melting of a layered crustal protolith: implications for the generation of anatetic granites. *Contributions to Mineralogy and Petrology* 114, 365–378.
- Vavra, G., Gebauer, D., Schmid, R., Compston, W. (1996) Multiple zircon growth and recrystallization during polyphase late carboniferous to triassic metamorphism in granulites of the Ivrea Zone (Southern Alps): An ion microprobe (SHRIMP) study. *Contributions to Mineralogy and Petrology* 122, 337–358.
- Voshage, H., Hunziker, J.C., Hofmann, A.W., Zingg, A. (1987) A Nd and Sr isotopic study of the Ivrea zone, Southern Alps, N-Italy. *Contributions to Mineralogy and Petrology* 97, 31–42.
- Watkins, J.M., Clemens, J.D., Treloar, P.J. (2007) Archaean TTGs as sources of younger granitic magmas: Melting of sodic metatonalites at 0.6–1.2 GPa. *Contributions to Mineralogy and Petrology* 154, 91–110.
- Weller, O.M., St-Onge, M.R., Rayner, N., Waters, D.J., Searle, M.P., Palin, R.M. (2016) U–Pb zircon geochronology and phase equilibria modelling of a mafic eclogite from the Sumdo complex of south-east Tibet: Insights into prograde zircon growth and the assembly of the Tibetan plateau. *Lithos* 262, 729–741.
- Yakymchuk, C., Brown, M. (2014) Consequences of open-system melting in tectonics. *Journal of the Geological Society* 171, 21–40.
- Yang, J., Xu, Z., Li, Z., Xu, X., Li, T., Ren, Y., Li, H., Chen, S., Robinson, P.T. (2009) Discovery of an eclogite belt in the Lhasa block, Tibet: A new border for Paleo-Tethys? *Journal of Asian Earth Sciences* 34, 76–89.

